Chair of Physical Metallurgy and Metallic Materials

Master Thesis

Impact of the stacking sequence on the stability of transition-metal diborides

Thomas Leiner, BSc

May 2021

This work received financial support from Austrian Science Fund (FWF): project number P30341-N36. The computational results presented have been achieved in part using the Vienna Scientific Cluster (VSC).

Affidavit:
I declare in lieu of oath, that I wroth this thesis and performed the associated research myself, using only literature cited in this volume.

Datum

Unterschrift

Acknowledgements

I want to thank everybody who made my university studies possible and joyful. Out of the many people who accompanied me during these years, I want to name a few here.

First of all I want to thank my parents, Karin and Gerhard, for their financial support during these years, which made it possible to attend the university in Leoben.

Secondly, I want to thank the supervisor of this thesis, Priv. Doz. David Holec PhD, for introducing me to the world of ab-initio calculations, the opportunity to write about a highly interesting group of materials, for bringing me into the CMS group, where I found many like-minded colleagues and for his relentless support in the creation of this work.

Lastly, I want to thank my girlfriend Alexandra for all the emotional support and for never stopping to believe in me.

Contents

Abstract

Abstract

Transition-metal diborides are a very hard and brittle type of materials, which, among others, find uses as protective coatings. The investigated diborides (Cr, Hf, Mn, Mo, Nb, Re, Ta, Ti, V, Zr) occur in three different known stackings.

In this work, these different stacking sequences of transition-metal diborides are explained and the impact of the stacking sequence on the stability of diborides is investigated via *ab initio* methods and phonon analysis.

Predictions about a possible stability of certain stackings were made and their behaviour was compared to each other.

Kurzfassung

Kurzfassung

Übergangsmetalldiboride sind eine sehr harte und sehr spröde Klasse von Materialien, welche, unter anderem, als Beschichtungen Einsatz finden. Die untersuchten Diboride (Cr, Hf, Mn, Mo, Nb, Re, Ta, Ti, V, Zr) kommen in drei verschiedenen, bekannten Stapelungen vor.

In dieser Arbeit werden die Stapelordnungen der Übergangsmetalldiboride erklärt und der Einfluss der Stapelordnung auf die Stabilität der Diboride mittels *ab initio* Methoden und Phononenanalyse untersucht.

Vorhersagen über eine mögliche Stabilität gewisser Stapelungen werden gemacht und deren Verhalten untereinander verglichen.

Chapter 1

Theoretical background

1.1 Metal diborides

1.1.1 Applications of MeB_2

There are some lesser known uses for transition metal diborides (MeB_2) such as catalysts [1] or for electroreduction of carbon dioxide[2]. But the main application field for MeB_2 is as coatings, because of their excellent heat conductivity, oxidation stability and wear resistance [3]. As an example for the multitude of possible uses, some of the applications for selected MeB_2 are listed in the following paragraphs.

TiB_2

TiB_2 is a stable material with very high melting point, high hardness and chemical inertness, as well as electric resistivity and thermal conductivity [4]. That is the reason why TiB_2 can be used as a coating for cutting tools, electric devices and wear parts. It has a low friction coefficient with aluminium which makes it a superb coating for cutting and drilling tools working [5]. In composite ceramics such as TiB_2-AlN it can also be used for drilling purposes [6]. It is used as a diffusion barrier in Ohmic contacts on Si or GaAS substrates [7]. Due to its inherent brittleness, multilayer coatings of TiB_2 and DLC (diamond-like carbon) are an ongoing topic of research [8].

HfB_2

HfB_2 is used as a coatings because of its high wear resistance and high resistance to oxidation [9]. In space flight applications, it is classified as ultra high temperature ceramic (UHTC), same as ZrB_2 and NbB_2, and it is used as heat shields [10]. Additionally, it is used as a high temperature composite material in combination with SiC [11].

MgB_2

Bulk superconductivity of MgB_2 at 39 K has been found in 2001 which, at the time, was the highest transition temperature for a non-copper-oxide bulk superconductor [12].

VB_2

VB_2 finds application in VB_2/air batteries, where it acts as an anode [13].

1.1.2 Motivation for the present Study

There is an ever increasing need to improve the characteristics of materials or to find a material which can fulfil the needed requirements while being produced at a cheaper cost. Only then can a material be competitive in the long run to others in the open market. Due to this external pressure, companies and countries alike tend to invest into researching new materials which can satisfy the demand of ever better physical properties.

As almost all ultra hard materials such as diamond or cubic BN are either exceedingly rare or need extreme temperatures and pressures for their fabrication, alternate materials are in high demand [14].

Because of their favourable properties, such as high hardness and incompressibility (e.g. ReB_2 which is said to have hardness comparable to that of diamond [15]), a question of how much of these properties are due to their unique crystallographic structure arises. Namely, the stability of these structures and possibility of metastable structures needs to be carefuly and consistently evaluated.

1.2 Atomic Structure

1.2.1 Atomic Structure

For the sake of simplicity, we can imagine an atom as a sphere, that takes takes up a certain amount of space, depending on its radius. Atoms tend to arrange themselves, when they are cooled below their respective melting temperature, into a periodic pattern. Usually they assume an arrangement which leads to as dense packing of the atoms as possible, to decrease their free surface and therefore the overall energy of the system.

The three most common stacking orders are the face-centred-cubic (fcc), the body-centred cubic (bcc) and hexagonal-close-packed (hcp). Out of those, the fcc and the hcp stacking differ only by the sequence the most densely packed planes of atoms are stacked above each other. While for the hcp stacking order, the planes are stacked in an "...ABAB..."

sequence (Fig. 1.1), the atoms in the fcc structure are stacked in an "...ABCABC..." pattern (Fig. 1.2) [16].

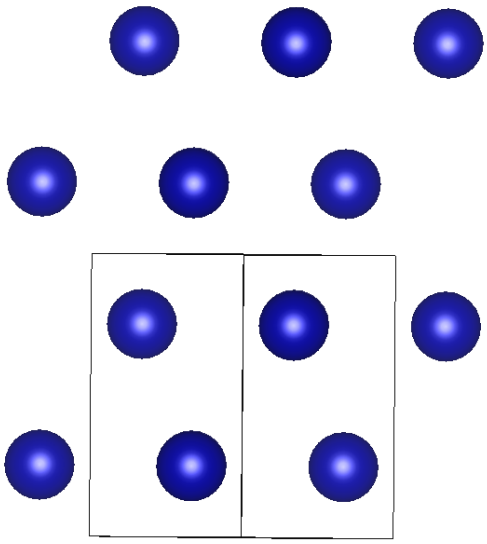

Figure 1.1: hcp stacking order along the [0001] direction (vertical, visualisation created with VESTA [17]).

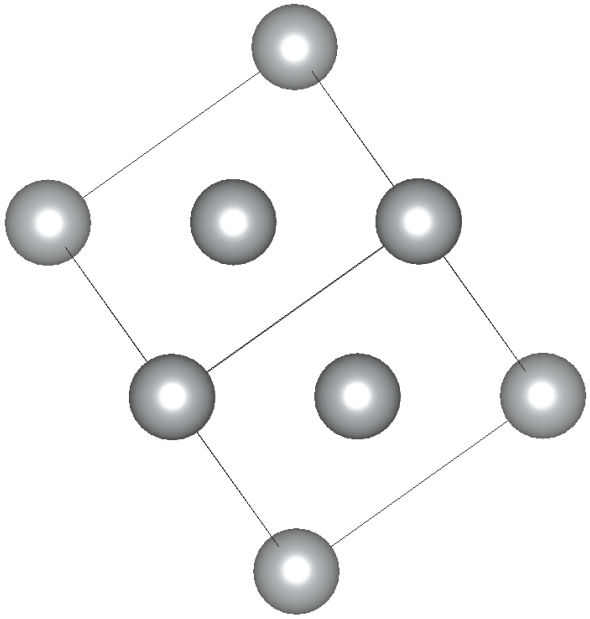

Figure 1.2: fcc stacking order along the ⟨111⟩ direction (vertical, visualisation created with VESTA [17]).

1.2.2 Stacking Faults

Stacking faults are two-dimensional defects in the crystal lattice. They arise when there is a deviation from the perfect periodic stacking. As an example we consider the stacking faults in an fcc material. There can either be a missing plane in the stacking order, or an additional plane of atoms. In the first case, an intrinsic stacking fault is created with the stacking order "...ABCA-BA-BC...", where BA is the stacking fault. In the second case, an extrinsic stacking fault occurs, with the stacking order "...ABCA-BAC-ABCA..." with BAC as the stacking fault. In conclusion, stacking faults in simple structures are additional or missing planes of atoms (Fig. 1.3) [16].

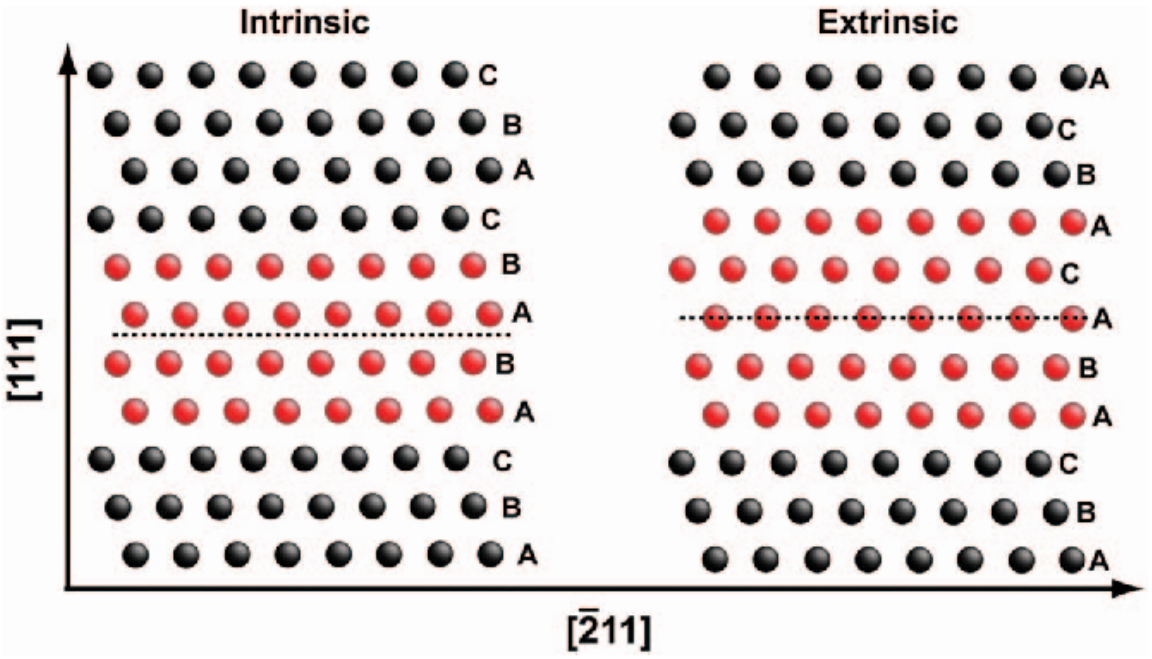

Figure 1.3: Intrinsic and extrinsic stacking faults in fcc (taken from [18]).

Impact of Stacking-Fault Energy on Mechanical Properties

The energy required to form a stacking fault is called stacking-fault energy (SFE), which plays a significant role in the mechanical properties of a material. It is noted as γ_{SFE} and its unit is energy per area (typically, J/m^2 or eV/Å^2). SFE determines the splitting of dislocations into partial dislocations: lower SFE results in an wider splitting of the partial dislocations and vice versa (Figs. 1.4 and 1.5). When the stacking fault energy is low, the wider splitting of the partial dislocations results in a lower mobility of dislocations, due to a lack of slip planes, and therefore a decreased ductility of the material. Therefore the preferred deformation mechanism for materials with very low SFE is twinning [16].

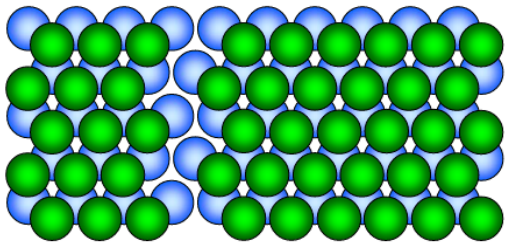

Figure 1.4: Perfect dislocation in an fcc crystal [19].

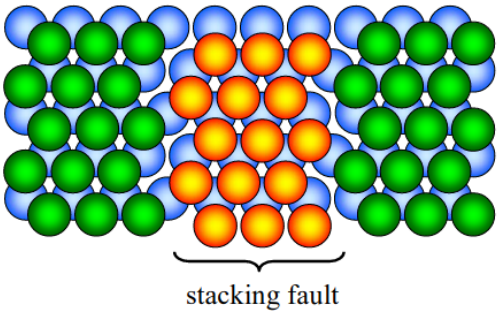

Figure 1.5: Partial dislocations separated by a stacking fault [19].

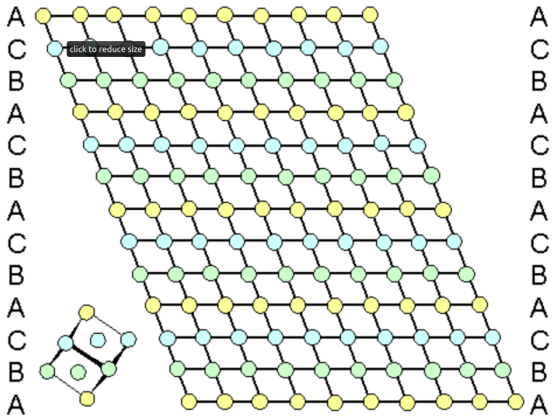

Figure 1.6: Perfect fcc crystal [21].

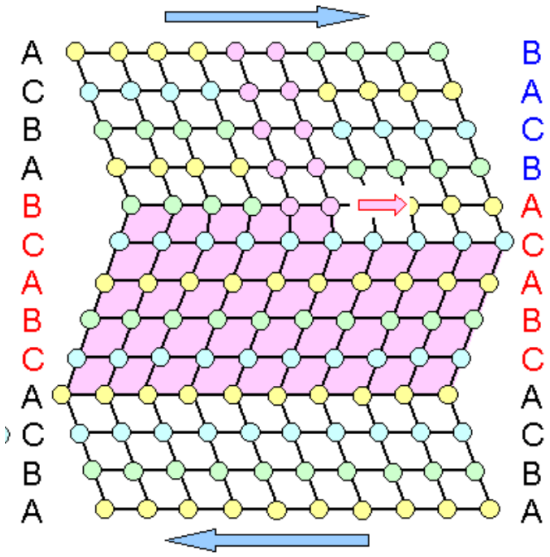

Figure 1.7: Deformation by twinning [21].

Twinning

When the crystals are sufficiently loaded with shear stress, they may deform plastically by twinning. During the twinning process, atoms move by translation over relatively small distances, where multiple rows of atoms are displaced along a glide plane. Hereby the stacking order of the twinned crystal (Fig. 1.7) is changed compared to the perfect crystal (Fig. 1.6); it exhibits the mirrored ordering of the crystal structure [20].

1.2.3 Phase Stability

A phase of a material is a region of space where the material has uniform physical properties. Therefore, we can easily differentiate between the solid, liquid and gas phase of a material.

This study will deal with different phases in solids. As an example we can take iron, which

at room temperature is stable in the bcc structure, called the α-phase. At elevated temperatures, the α-phase transforms into the γ-phase. The phase stabilility can be shown using phase diagrams, example of which is the the Fe-Fe_3C phase diagram shown in Fig. 1.8. The full lines separate the metastable phases of the Fe-Fe_3C with the carbon bound in the cementite phase (Fe_3C), while the dashed lines show the phase diagram corresponding to the stable Fe-C system, where carbon is found as stable graphite. The reason for the existence of metastable Fe_3C are finite cooling speeds which do not allow the thermodynamically stable graphite phase to form due to slower kinetics at lower temperatures. An unstable phase will instantly transform into either a metastable or stable configuration [16].

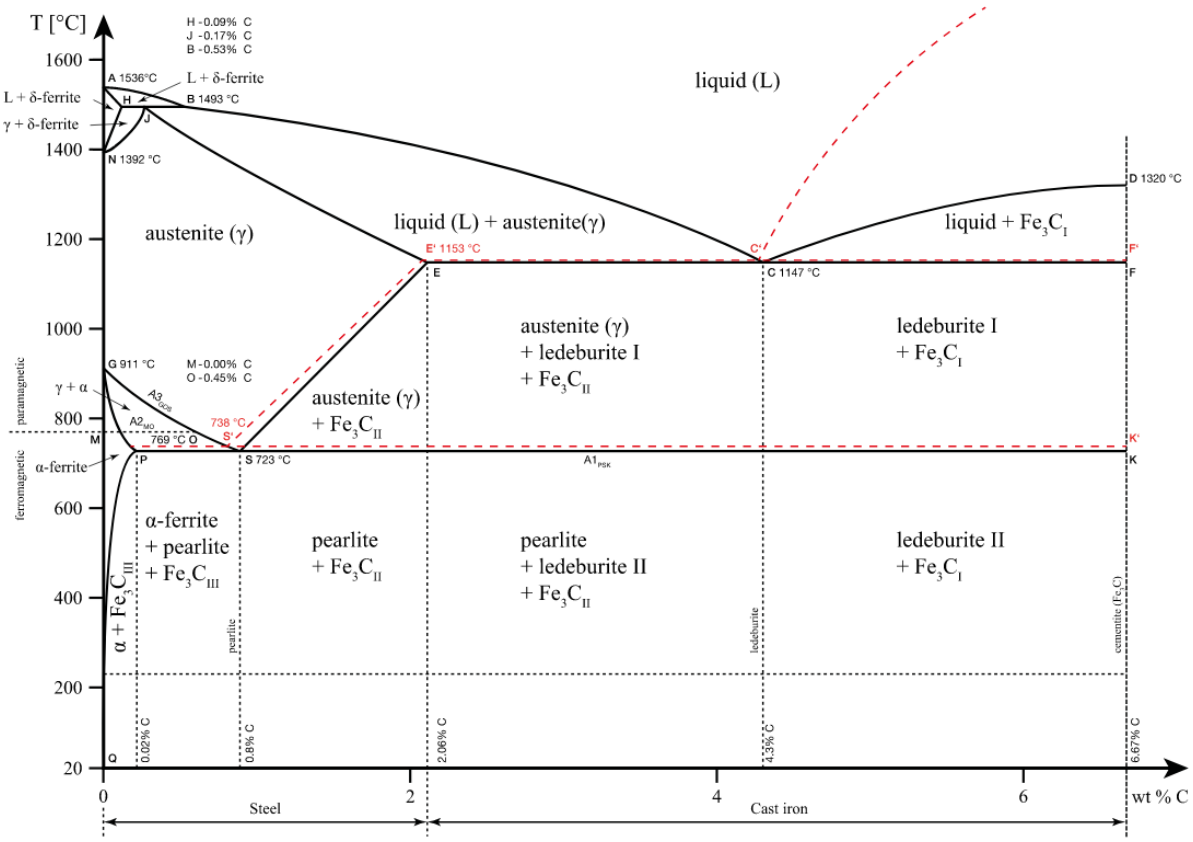

Figure 1.8: Fe-Fe_3C phase diagram (taken from [22]).

1.2.4 Structures of MeB_2

In this work, transition metal diborides from TiB_2 to ReB_2 (excluding TcB_2, because of its radioactivity) in the periodic table were studied. These come in three different stable structures. WB_2 crystallised in the ω-structure (space group 194, $P6_3/mmc$) as seen in Fig. 1.9, ReB_2 in the ReB_2-structure (space group 194, $P6_3/mmc$) as seen in Fig. 1.10, and all other MeB_2 in the α-structure (space group 191, $P6/mmm$) as seen in Fig. 1.11.

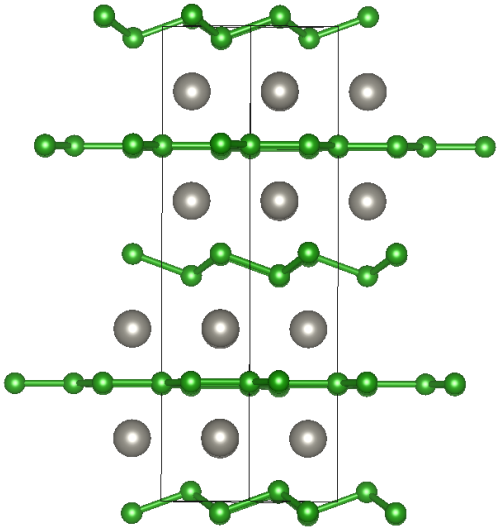

Figure 1.9: ω-structure of WB_2 (visualised with VESTA [17]).

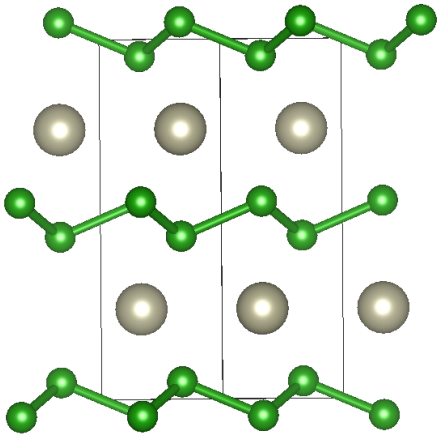

Figure 1.10: Structure of ReB_2 (visualised with VESTA [17]).

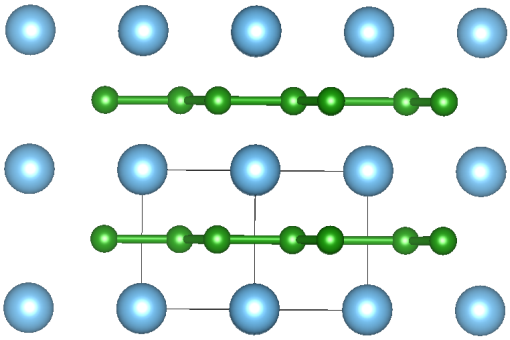

Figure 1.11: α-structure of TiB_2 (visualised with VESTA [17]).

Noticeably, the boron sheets between the metal atom planes come in two configurations, either flat (H) as in the α-structure or puckered (K) as in the ReB_2-structure or alternating as in the ω-structure. The metal atoms are either in an A-A-A-A stacking sequence for the α-structure, an A-B-A-B stacking sequence for the ReB_2-structure, or the A-A-B-B stacking sequence for the ω-structure. This leads us to the following stacking sequence for the three structures [23]:

MeB_2: ...A-H-A-H...
ReB_2: ...A-K-B-K-A-K...
WB_2: ...A-H-A-K-B-H-B-K...

1.3 Density Functional Theory

1.3.1 The Schrödinger Equation

In essence, all quantum mechanical processes revolve around the Schrödinger equation:

$$H\psi = E\psi \ . \tag{1.1}$$

By applying the Hamiltonian operator, H, on the wave function, it is possible to calculate the energy levels of the system (eigenvalues of H). This may sound simple in theory, but we are only able to directly calculate it for the most simple of systems, such as single atoms. For bigger systems, for example a solid crystal, we have to take certain approximations to find the lowest energy level and therefore ground state structure for our system. The approach employed here is based on Density Functional Theory (DFT) which shall be explained in the following paragraphs. The underlying mathematics were for the most part omitted and the theory was intentionally simplified, to get a better understanding how DFT works instead of deriving why it works the way it does [24, 25].

1.3.2 Electron density

Due to the uncertainty principle, electrons are particles which cannot be fully localised in a crystal structure. Instead, they have a probability to be found at a certain point in the crystal. This probability is called the *electron density*, which in turn is the wave function of the electrons squared. Therefore, by taking the Schrödinger equation (Eq. (1.1)) into account, we can immediately see that knowing the electron density is of the utmost importance to know the corresponding wave function, and to be finally able to calculate its energy [24, 25].

1.3.3 Hartree and Hartree-Fock methods

Before the emergence of DFT, the Hartree and the Hartree-Fock (HF) methods were the way to calculate the many-electron problems. Due to the complexity of solving the Schrödinger equation for multiple electrons (an n-electron system), the early methods of solving it relied on the simplifying the interacting n-electron system into a system where the electrons no longer interacted with each other and only "felt" the presence of the other electrons as a mean field. The interacting n-electron system therefore became a non-interacting one-electron system which could be solved by limited computational resources, by solving one electron at a time [24, 25].

With these simplifications, Hartree introduced the self-consistent field method to solve the wave equation:

$$(-\frac{\hbar^2}{2m}\nabla^2 + U_{\text{ext}}(r) + U_H(r))\psi(r) = E\psi(r) \ , \tag{1.2}$$

where E_{ext} is the attractive interaction between electrons and nuclei and U_H is the Hartree potential coming from the classical Coulomb repulsive interaction between each electron and the mean field.

Due to the simplifications of the Hartree method, it fails to fulfil the Pauli exclusion principle. To resolve this, the method has been refined into the Hartree-Fock (HF) method. Here, the n-electron wave function is approximated by a linear combination of non-interacting wave functions in the form of a Slater determinant. This solution leads to the following energy contributors to the total energy E:

$$E = E_{\text{kin}} + E_{\text{ext}} + E_H + E_X \ . \tag{1.3}$$

Here, E_{kin} is the kinetic energy of the electrons and E_X the exchange energy coming from the anti-symmetrical nature of the wave function in the Slater determinant form [24, 25].

1.3.4 The Hohenberg-Kohn Theorems

Hohenberg and Kohn showed that the electron density can be used as a central quantity to replace the wave function, and thus formulated the modern Density Functional Theory (DFT). They managed to mathematically connect the electron density, wave function, external energy and Hamiltonian with the use of their theorems.

The first theorem states that there is an unique external potential (U_{ext}) acting on the electrons which is solely determined by the ground state electron density.

U_{ext} is by definition the measure of the interaction between electrons and nuclei, while the term "external" refers to the viewpoint of the electron. This Coulomb attraction by the nuclei is by nature dependent on their charge and distance and therefore the external potential, and corresponding energy E_{ext}, is system dependent.

The internal energy, E_{int}, consists of the kinetic energy of the electrons and of the electron-electron interactions. This contribution is independent of nuclei and hence it is system independent. Therefore, once known, it can be applied to any system at will.

As E_{int} is system independent, different Hamiltonians differ only by their external energies, which, as stated above, is solely determined by the electron density.

In conclusion this means that the electron density defines Hamiltonian, wave function and external energy and all ground-state properties of the system. Consequently, with the electron density we can calculate, e.g., the total energy of a system, among other properties. This forms the basis of all DFT calculations.

Their second theorem states, that we can approach the ground state energy of a system by varying the electron density for a given external potential (and hence fixed Hamiltonian).

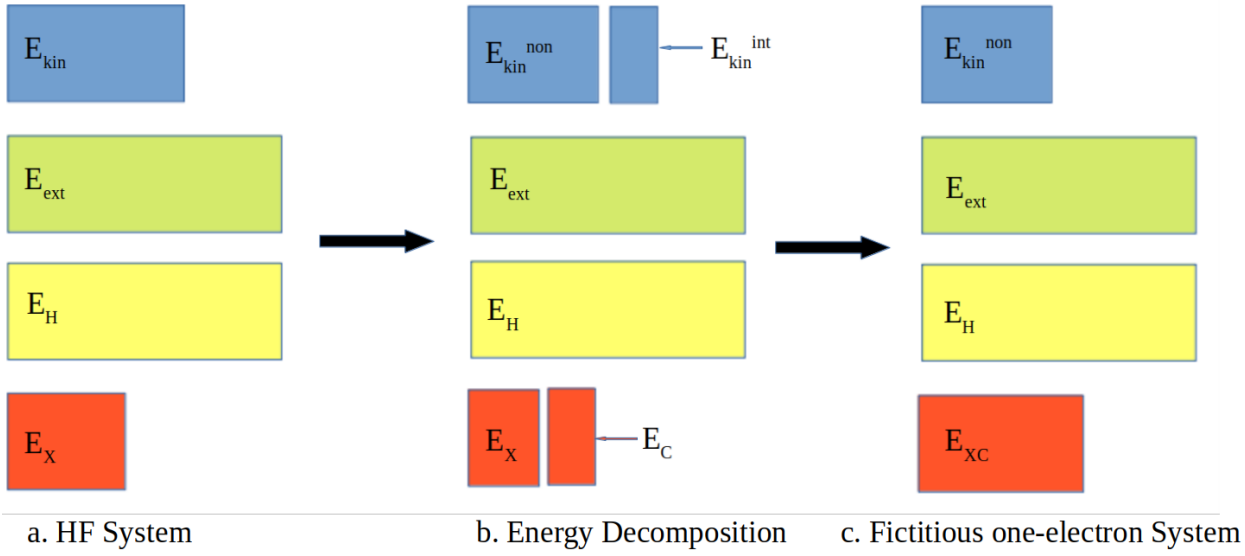

Figure 1.12: Energy contributions in the Kohn-Sham approach (taken from [25]).

This process is called variational principle and the electron density, at which the energy is at a minimum, is the true ground-state electron density. The process is a step by step process, where we try to get closer and closer to the ground state energy [24, 25].

1.3.5 The Kohn-Sham approach

The Kohn-Sham approach starts by taking the kinetic, external, Hartree and exchange energies into consideration. Let us start with the HF total energy, Eq. (1.3). In a system with multiple electrons (n-elecrons) it is very hard to calculate the coupled interactions between electrons. Therefore, Kohn and Sham proceeded by splitting the energy terms up into interacting and non-interacting terms:

$$E_{\text{kin}} = E_{\text{kin}}^{\text{non}} + E_{\text{kin}}^{\text{int}} \ . \tag{1.4}$$

Moreover, additional energy term, E_C^{int}, enters the total energy. This is correlation energy and it is neglected in the HF method.

By summing up all interacting terms into E_{XC}:

$$E_{XC} = E_X + E_C^{\text{int}} + E_{\text{kin}}^{\text{int}} = E_X + E_C \ , \tag{1.5}$$

we arrive at formula:

$$E = E_{\text{kin}}^{\text{non}} + E_{\text{ext}} + E_H + E_{XC} \ . \tag{1.6}$$

While $E_{\text{kin}}^{\text{non}}$, E_H and E_{ext} are relatively easy to calculate while E_{XC} has to be approximated. By doing this, every single electron can be seen as independent from the other electrons,

which simplifies the problem from an interacting n-electron system to a non-interacting n one-electron problems. Such transformation enables us able to calculate bigger systems with many electrons. All that is left to be figured out is how to deal with E_{XC}.

According to Eq. (1.5) the exchange-correlation energy is made up of the correlation energy (E_C) and the exchange energy (E_X). The E_{XC} contains all quantum mechanical effects.

The E_X is the exchange energy between electrons of the same spin, which stems from the Pauli exclusion principle. It leads to an anti-symmetry of the orbitals and their orthogonal arrangement in space. The reduced electron density stemming from this effect is called the *exchange hole*.

E_C is the correlation energy between electrons with different spin, which stems from the fact that the electrons with the same charge repel and therefore avoid each other. This leads to a lower electron density around the electron, which is called a *correlation hole*.

The exchange hole and the correlation hole together form the *exchange-correlation* hole. The exchange energy and therefore the exchange hole is the main contributor for the high electron densities due to the Pauli exclusion principle which becomes more significant with higher electron densities and the correlation energy therefore becomes more significant for lower electron densities [24, 25].

1.3.6 LDA and GGA

Two common approximations for the exchange and correlation energy shall be described here, the local density approximation (LDA) and the generalised gradient approximation (GGA).

The LDA works by substituting a real, gradually changing electron density of a system with local elements of uniform electron density. By doing so the system is divided into regions of different but constant electron density. In each of these elements the exchange-correlation energy can be calculated and ultimately summed up to get the total exchange-correlation energy of the system.

LDA usually underestimates the exchange energy and overestimates the correlation energy by roughly the same amount, which makes LDA a decent approximation for the exchange and correlation energy. However, it typically leads to overestimation of binding, and hence underestimation of interatomic spacings.

The GGA goes one step further than the LDA by adding the gradient of the electron density to the local electron density as an input parameter. This leads, in general, to more accurate XC calculations than with just LDA, while it still tends to overestimate bonding length and underestimates band gaps [24, 25].

1.4 Software packages

Below is a short overview of the software tools used in this thesis.

1.4.1 VASP code

"VASP is a complex package for performing ab-initio quantum-mechanical molecular dynamics (MD) simulations using pseudopotentials or the projector-augmented wave method and a plane wave basis set. The approach implemented in VASP is based on the (finite-temperature) local-density approximation with the free energy as variational quantity and an exact evaluation of the instantaneous electronic ground state at each MD time step." [26]

VASP has its roots in the CASTEP code, which was in 1989 brought to the Vienna University by Jürgen Hafner. In 1995, VASP had become a stable and versatile tool for *ab initio* calculations and has been improved ever since. VASP is currently developed by Georg Kresse and his team [27].

The pseudopotentials used in this work are:

Boron:	PAW_PBE B 06Sep2000
Chromium:	PAW_PBE Cr_pv 02Aug2007
Hafnium:	PAW_PBE Hf_pv 06Sep2000
Manganese:	PAW_PBE Mn_pv 02Aug2007
Molybdenum:	PAW_PBE Mo_pv 04Feb2005
Niobium:	PAW_PBE Nb_sv 25May2007
Rhenium:	PAW_PBE Re_pv 06Sep2000
Tantalum:	PAW_PBE Ta_pv 07Sep2000
Titanium:	PAW_PBE Ti 08Apr2002
Vanadium:	PAW_PBE V 08Apr2002
Tungsten:	PAW_PBE W 08Apr2002
Zirconium:	PAW_PBE Zr_sv 04Jan2005

For the entire work, an automatically generated k-point mesh with length parameter 50 Å was used.

1.4.2 Gadget code

GADGET is a program for efficient atomic and lattice relaxation, developed by Tomáš Bučko [28].

Examples for the input data used with the GADGET code are given below. While using GADGET, the INCAR file is similar to that used during usual VASP calculations.

INCAR:

```
ALGO = Fast
EDIFF = 1e-06
EDIFFG = 0.0001
ENCUT = 500
IBRION = -1
LCHARG = False
LREAL = False
LWAVE = False
NCORE = 8
NSW = 0
PREC = Accurate
```

When using GADGET, controlling the relaxation by setting the correct constraints is crucial. These constraints are specified in the ICONST file. Note, that in the example given below the constraints are specified in a way that constrains the cell to keep its hexagonal structure.

ICONST

```
LA: 0 2
LA: 0 1
LA: 1 2
RatioLR: 0 1
fX: 0:S
fY: 0:S
fX: 1:S
fY: 1:S
fX: 2:S
fY: 2:S
fX: 3:S
fY: 3:S
```

1.4.3 VESTA

VESTA is a 3D visualisation program for structural models, volumetric data such as electron/nuclear densities, and crystal morphologies [17].

1.4.4 Phonopy

Phonopy is an open source package for phonon calculations at harmonic and quasi-harmonic approximation levels [29].

The supercells needed for the Phonopy calculation were created, from already existing 1x1x4 cells, with a random displacements method according to the input file:

```
DIM = 4 4 1

PRIMITIVE_AXES = AUTO

ATOM_NAME = Re O

ATOM_NAME = B 1

ATOM_NAME = B 2

CELL_FILENAME = POSCAR

CREATE_DISPLACEMENTS = .TRUE.

RANDOM_DISPLACEMENTS = 2

DISPLACEMENT_DISTANCE = 0.03

PM = .TRUE.

DOS = .TRUE.

tolerance=1e-4
```

The phonon branches were calculated with the ALM force calculator and plotted according to this specification:

```
FC_CALCULATOR = ALM

DIM = 4 4 1

BAND = 0 0 0        1/3 1/3 0        1/2 0 0        0 0 0        0 0 1/2        1/3
1/3 1/2        1/2 0 1/2        0 0 1/2

EIGENVECTORS=.TRUE.
```

An example for the INCAR file (VASP master input file) used in the phonon calculation is given here:

```
PREC = Accurate
IBRION = -1
NELMIN = 5
ENCUT = 500
EDIFF = 1.000000e-08
ISMEAR = 0
SIGMA = 1.000000e-02
IALGO = 38
LREAL = .FALSE.
LWAVE = .FALSE.
LCHARG = .FALSE.
```

Chapter 2

Methods and Results

2.1 Convergence Tests

All the calculations using VASP have to meet certain criteria for them to converge and therefore give reasonable results within a small, but acceptable, margin of error. Usually, this error should be within 2 meV/at. in the present calculation. The two most important setting parameters to control this accuracy are the plane-wave cut-off energy (ENCUT set in the INCAR input file) and the number of k-points (specified in the KPOINTS file). The cut-off energy specifies to include in the basis set all plane-waves with a kinetic energy smaller than the specified value. As we are looking for the ground state solution of the problem, we can cut off the free electron solutions with an too high energy. namely with energy higher than the specified cut-off energy. The KPOINTS specify the Bloch vectors that will be used to sample the Brillouin zone of the calculation. The convergence tests for the studied transition-metal diborides (MeB_2) suggest that the desired accuracy is reached at an ENCUT of 500 eV and at k-points density corresponding to the length parameter $R_k = 50$ Å. as indicated by the yellow 2 meV/at. contour line seen at the xy-plane of the 3D graph. An example, in this case TiB_2, of the results of these calculations can be seen in Fig. 2.1. It has to be noted, that a higher value of ENCUT and KPOINTS increase the calculation time significantly. Therefore, it is desirable to find a compromise for their values to reach good results (as high values as possible) in a reasonable time frame (as small values as possible).

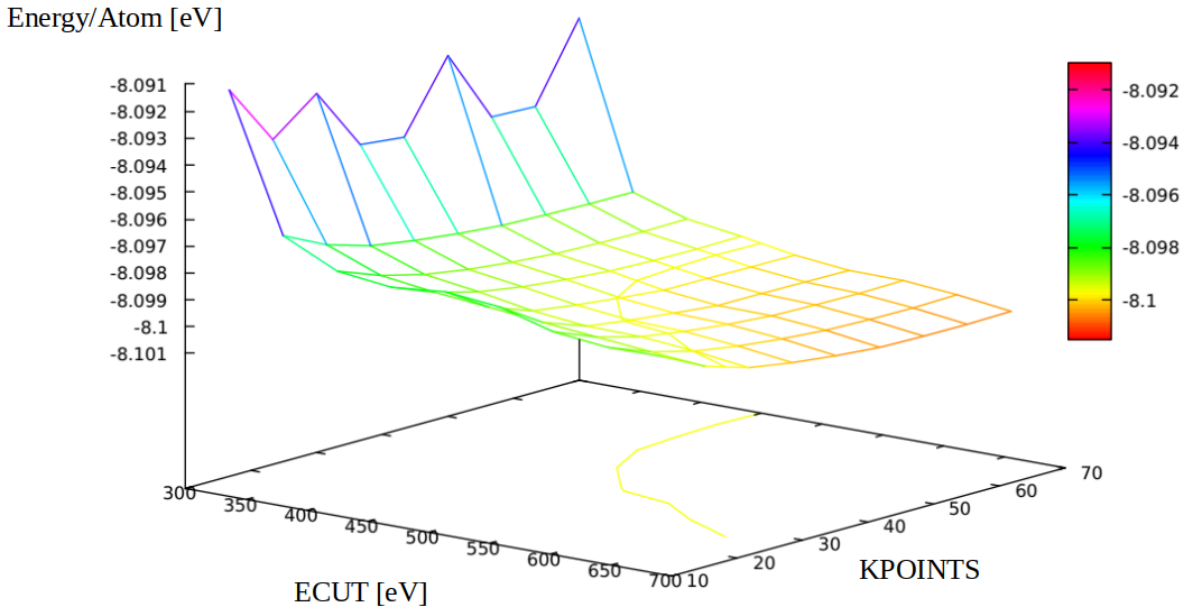

Figure 2.1: Example of a convergence test of TiB_2. Region in which the overall total energy (vertical axis) changes less than 2 meV/at. is marked by the yellow contour line. Energy cut-off energy (ECUT) is given in eV. density of k-points is characterised by a length parameter (KPOINTS) given in Å.

2.2 Energy Landscape Curves/Relaxation

In this part is reported the behaviour of the MeB_2 in terms of the energy landscape, when we shear them from their stable configurations (e.g., A-A-A-A) to the stacking order of those of other MeB_2. The results below were achieved by shifting metal atoms using multiple in-between steps from A to B position or vice-versa. At each step, the atoms were allowed to relax in the z-direction. while movement of the atoms in the x- and y-directions was prevented to keep the stacking order fixed. The transformation path was chosen as:

$$\text{A-A-A-A} \rightarrow \text{B-A-A-A} \rightarrow \text{B-A-B-A} \rightarrow \text{A-B-B-A} \rightarrow \text{A-A-A-A} \ . \tag{2.1}$$

The resulting energy per atom of the system was plotted on the vertical axis and the stacking order of the atoms (configuration of the supercell) on the horizontal axis in the graphs below (Figs. 2.3–2.13).

In most cases we can observe several local minima and thereby potential metastable structures. The global minimum is at the stacking order which corresponds to the stable structure. The other local minima are typically at other A or B stackings of the metal planes, but in some cases local minima are predicted also for lateral shifts between the A and B configurations.

In the cases of TiB_2 (Fig. 2.10) an VB_2 (Fig. 2.11) at the A-B-B-A stacking we can see two different energy states. The higher energy state was caused by the boron atoms being locked in a higher symmetry configuration and hence preventing them from relaxing to the lower energy state. By choosing a different starting position for the B atoms, the structure is able to relax into an lower energy state.

In any two neighbouring stackings (A-A-A-A, B-A-A-A, B-A-B-A or A-B-B-A) both correspond to a local energy minima, the energy difference between the initial (in terms of the transformation path Eq. (2.1)) and the local maximum between the two minima defines an energy barrier. For example, "barrier 1" corresponds to the energy difference between the local maximum between A-A-A-A and B-A-A-A and E(A-A-A-A), provided that both A-A-A-A and B-A-A-A configurations are local energy minima. This barrier must be overcome in order to proceed further along the transformation path. All barriers for all investigated MeB_2 are summarised in Fig. 2.2. The energies of all important configurations are given in Tab. 2.1.

Table 2.1: Total energies (in eV/at.) of important stacking along the transformation path, and corresponding energy barriers.

	CrB_2	HfB_2	MnB_2	MoB_2	NbB_2	ReB_2	TaB_2	TiB_2	VB_2	WB_2	ZrB_2
A-A-A-A	−7.9712	−8.7999	−7.6186	−8.1294	−8.6079	−8.1225	−9.0516	−8.1014	−8.1808	−8.6319	−8.3258
E-Barrier	−7.8528	−8.5172	−7.5805	−7.8739	−8.4087		−8.8979	−7.8147	−7.9495	−8.6059	−8.0431
B-A-A-A	−7.8893	−8.5282	−7.6108	−7.9869	−8.4345	−8.6023	−8.9307	−7.8284	−7.9680	−8.7400	−8.0573
E-Barrier	−7.7100		−7.5207	−7.8376	−8.2122	−8.5882	−8.7261	−7.5395	−7.7219		−7.7714
B-A-B-A	−7.7408	−8.2498	−7.5843	−7.9636	−8.2258	−9.0275	−8.7440	−7.5527	−7.7356	−9.0588	−7.7850
E-Barrier	−7.6824		−7.4692		−8.2188	−8.5287	−8.7302	−7.5447	−7.7316	−8.7571	−7.7759
A-B-B-A	−7.6902	−8.5336	−7.4771	−8.0507	−8.4885	−8.5931	−8.9949	−7.8417	−8.0266	−9.1464	−8.0619
E-Barrier	−7.6743	−8.5299	−7.4629	−7.9868	−8.4563		−8.9431	−7.8367	−8.0036	−8.6319	−8.0591
A-A-A-A	−7.9712	−8.7999	−7.6186	−8.1294	−8.6079	−8.1225	−9.0516	−8.1014	−8.1808	−8.6319	−8.3258
Barrier1	0.1185	0.2827	0.0381	0.2554	0.1992		0.1537	0.2867	0.2313	0.0259	0.2827
Barrier2	0.1793		0.0900	0.1492	0.2223	0.0140	0.2046	0.2889	0.2460		0.2859
Barrier3	0.0584		0.1151		0.0070	0.4988	0.0138	0.0080	0.0040	0.3017	0.0090
Barrier4	0.0159	0.0036	0.0142	0.0640	0.0322		0.0518	0.0050	0.0230	0.5145	0.0028

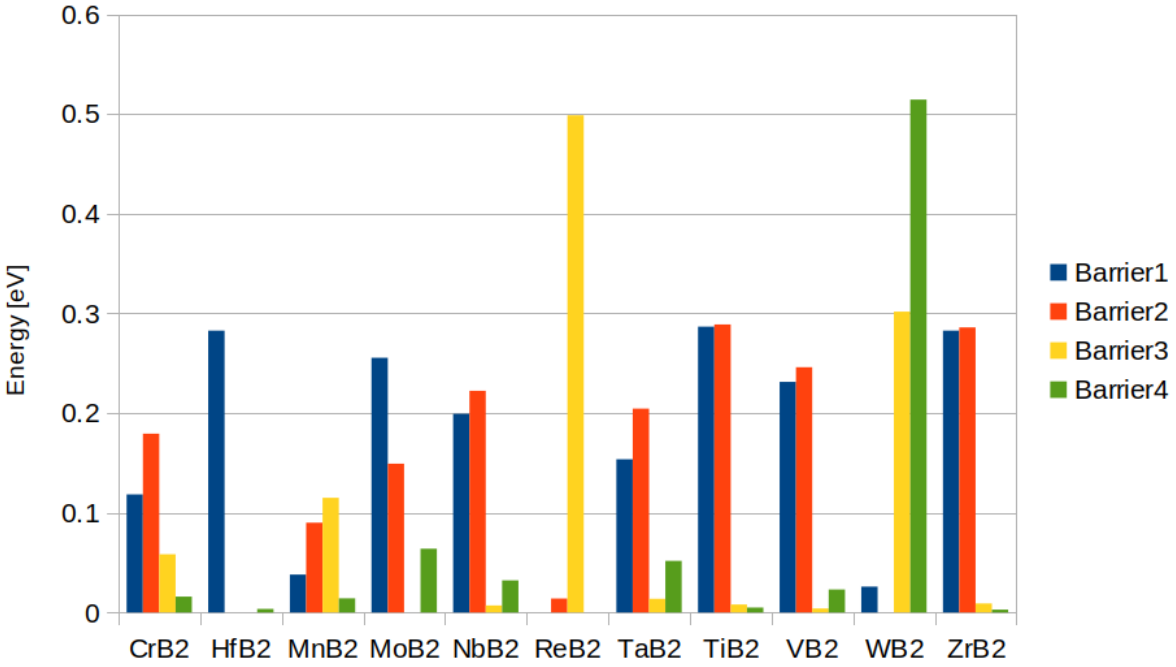

Figure 2.2: Energy barriers between different stacking orders of MeB_2.

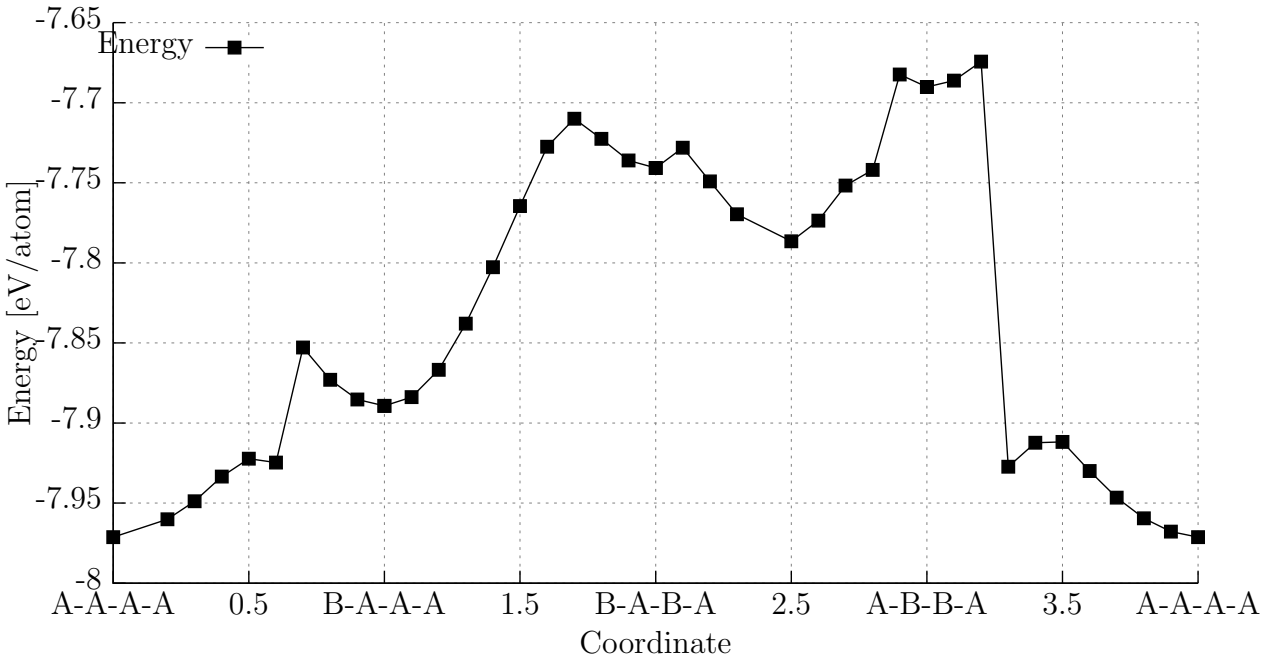

Figure 2.3: Total energy landscape for CrB_2.

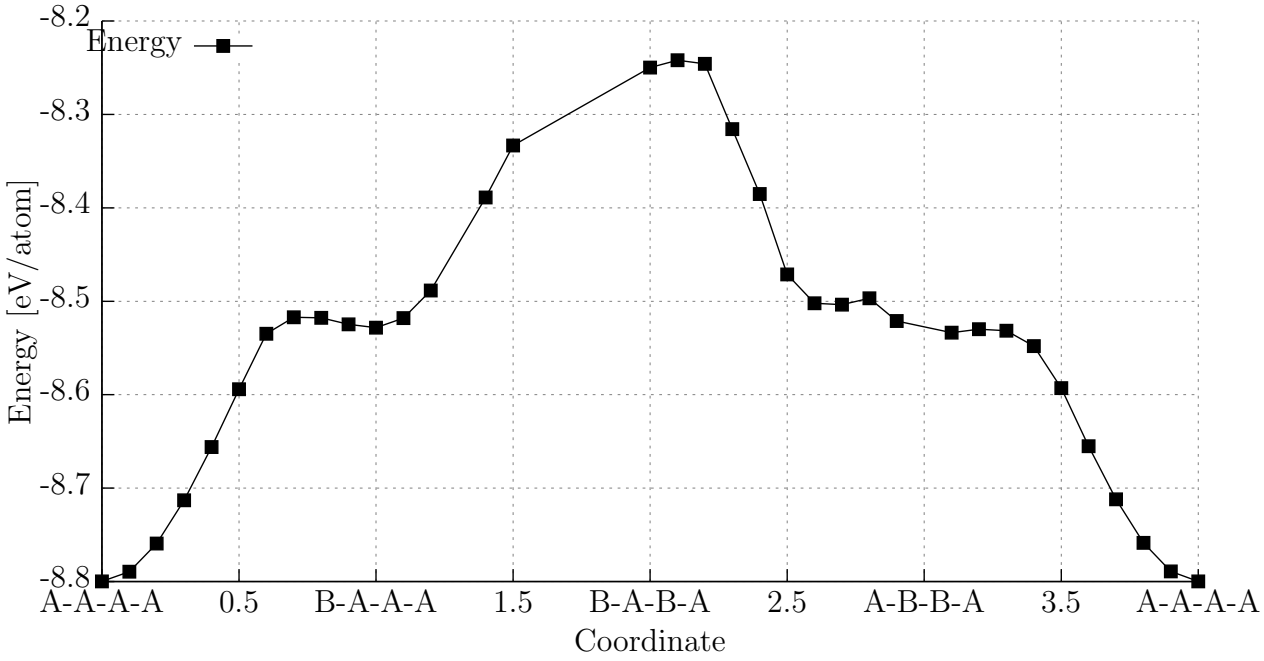

Figure 2.4: Total energy landscape for HfB_2.

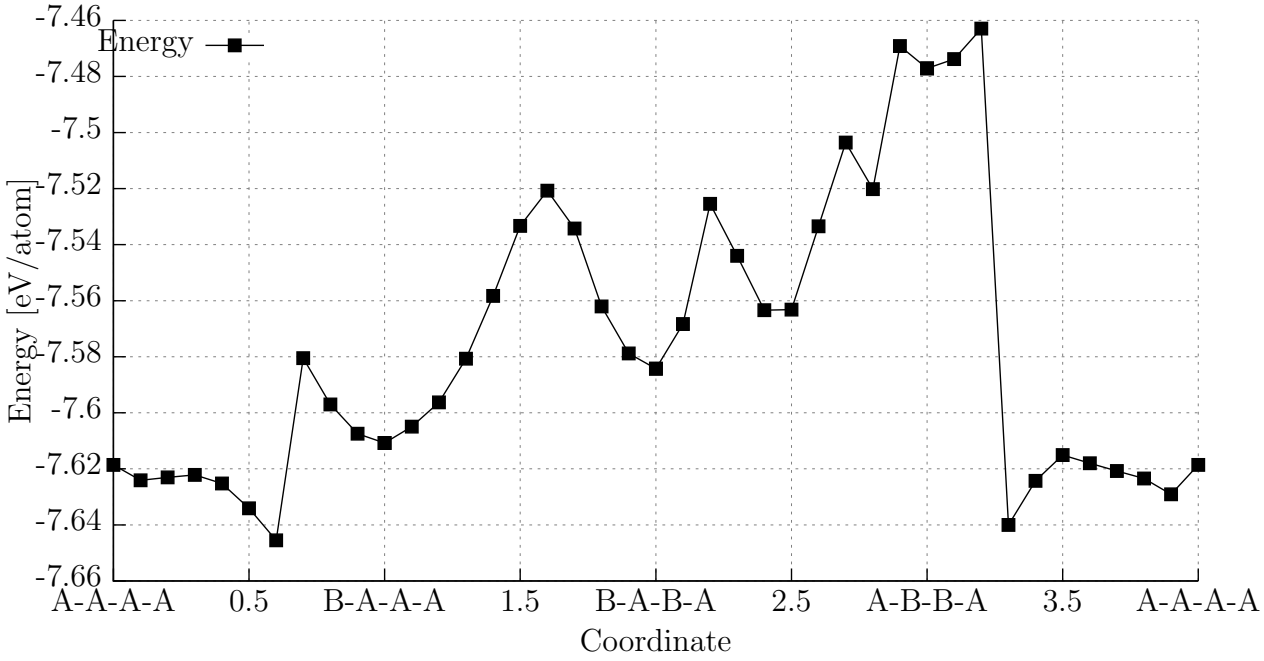

Figure 2.5: Total energy landscape for MnB_2.

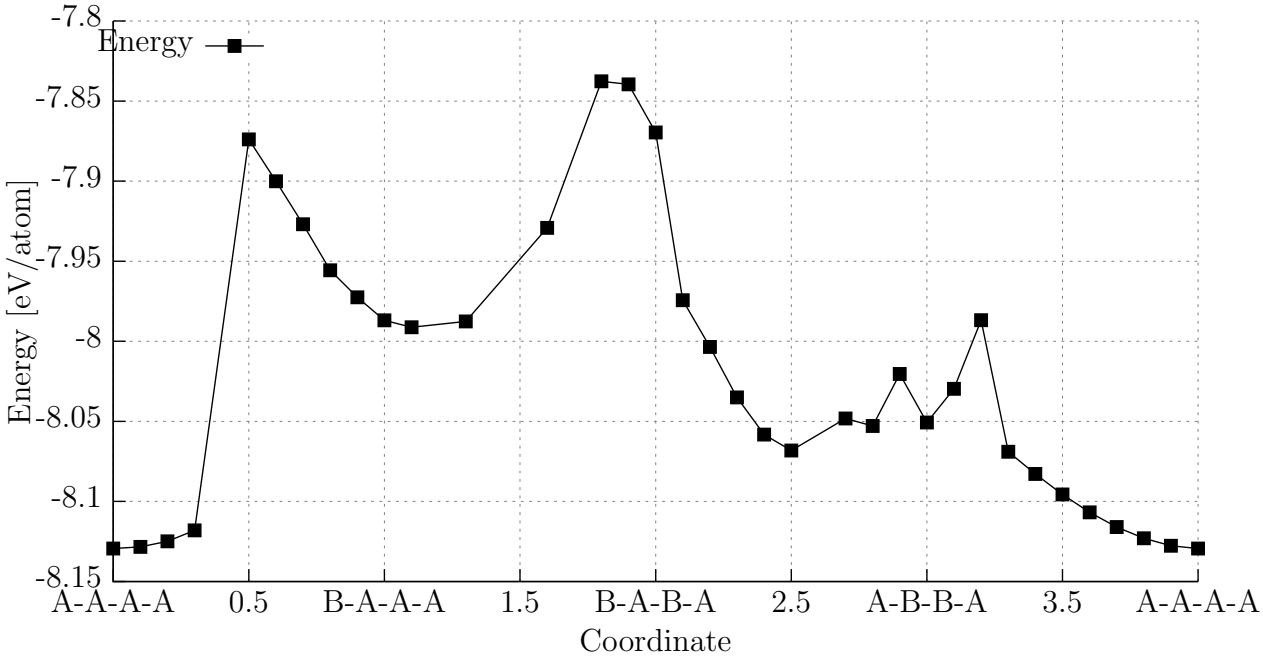

Figure 2.6: Total energy landscape for MoB_2.

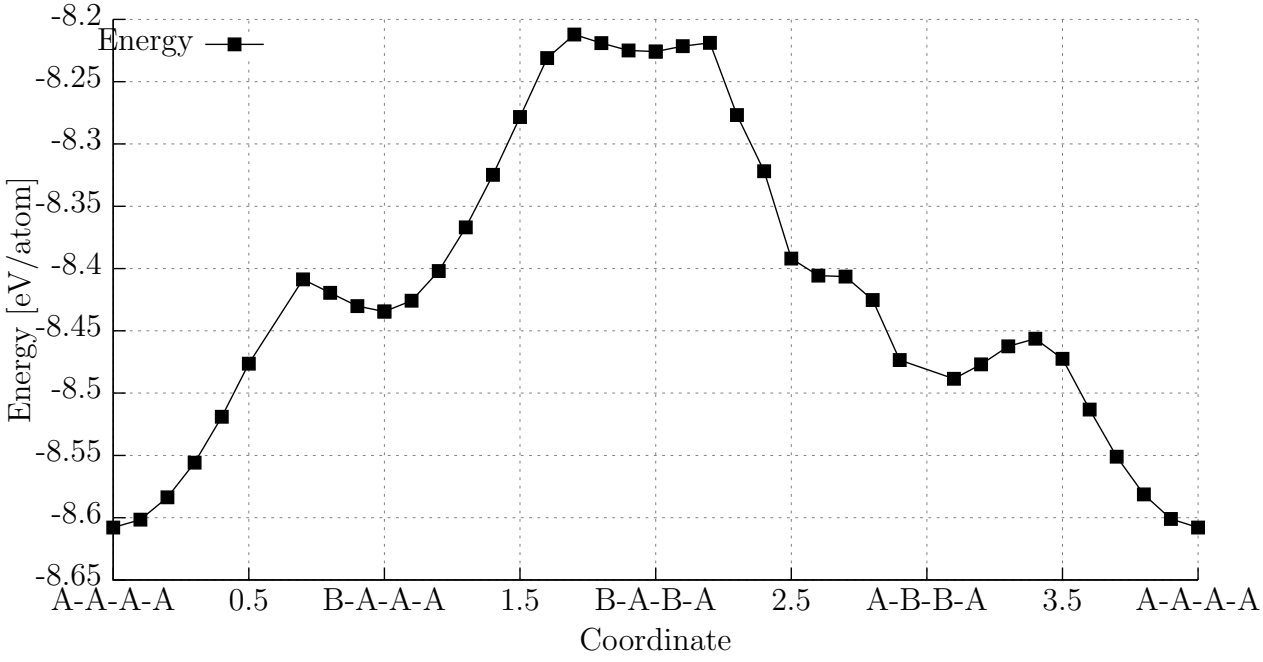

Figure 2.7: Total energy landscape for NbB_2.

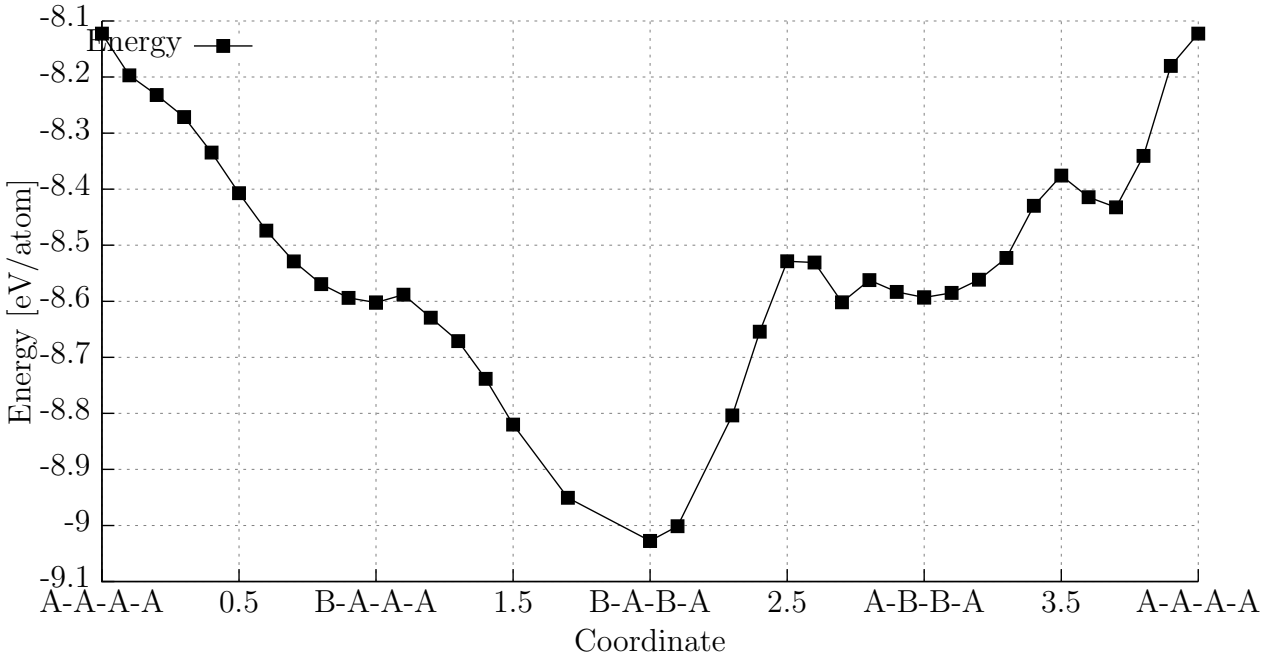

Figure 2.8: Total energy landscape for ReB_2.

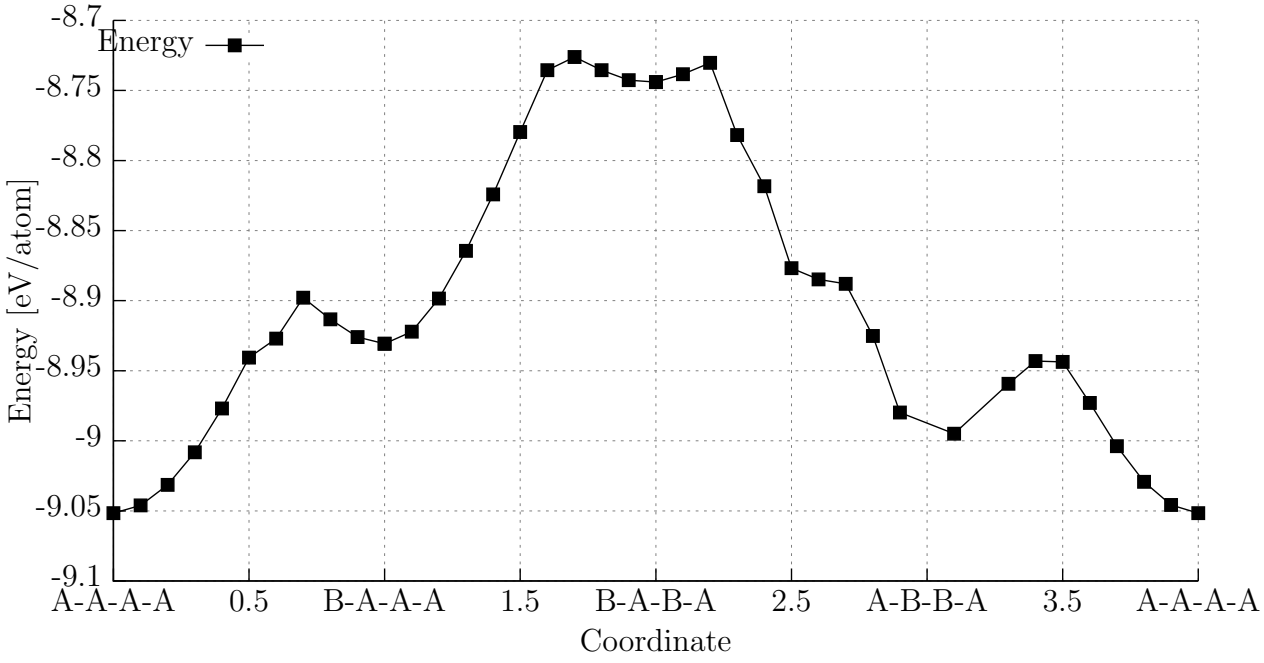

Figure 2.9: Total energy landscape for TaB_2.

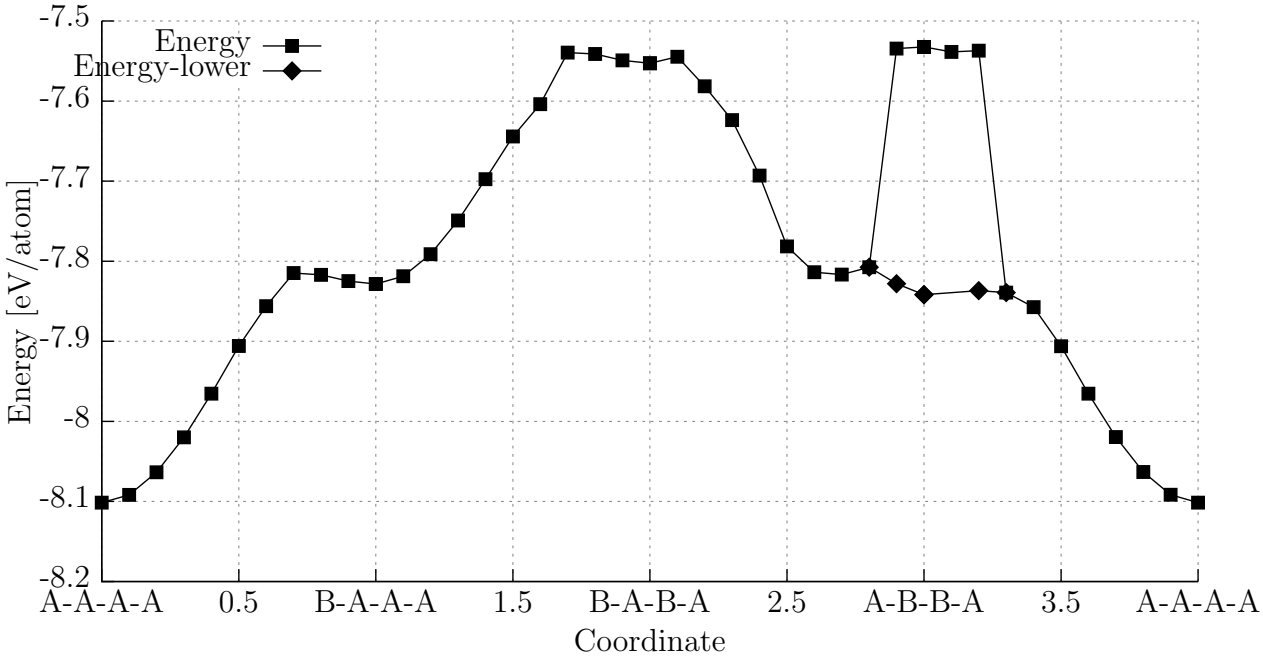

Figure 2.10: Total energy landscape for TiB_2.

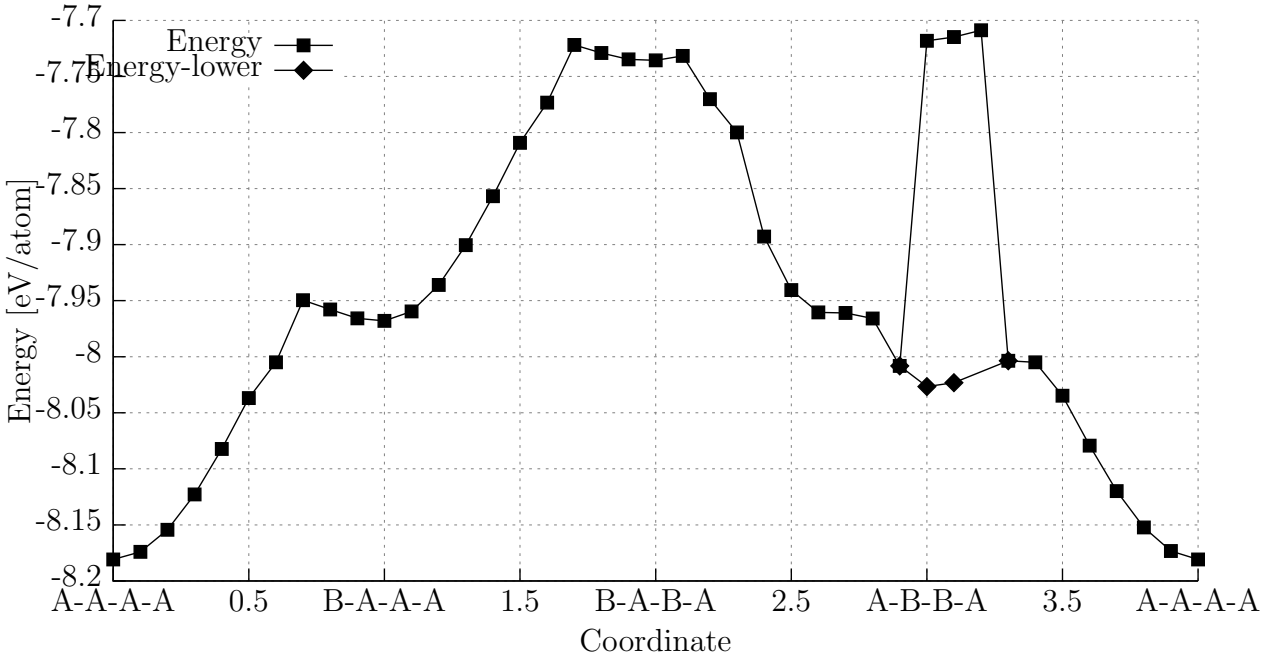

Figure 2.11: Total energy landscape for VB_2.

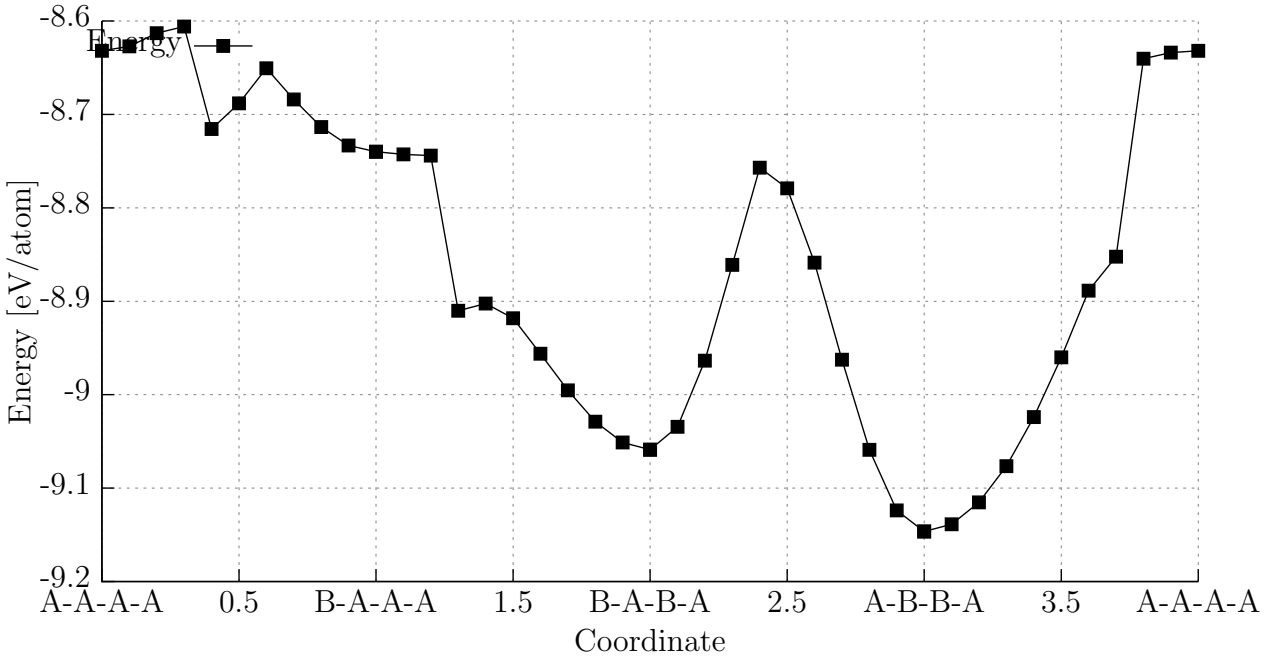

Figure 2.12: Total energy landscape for WB_2.

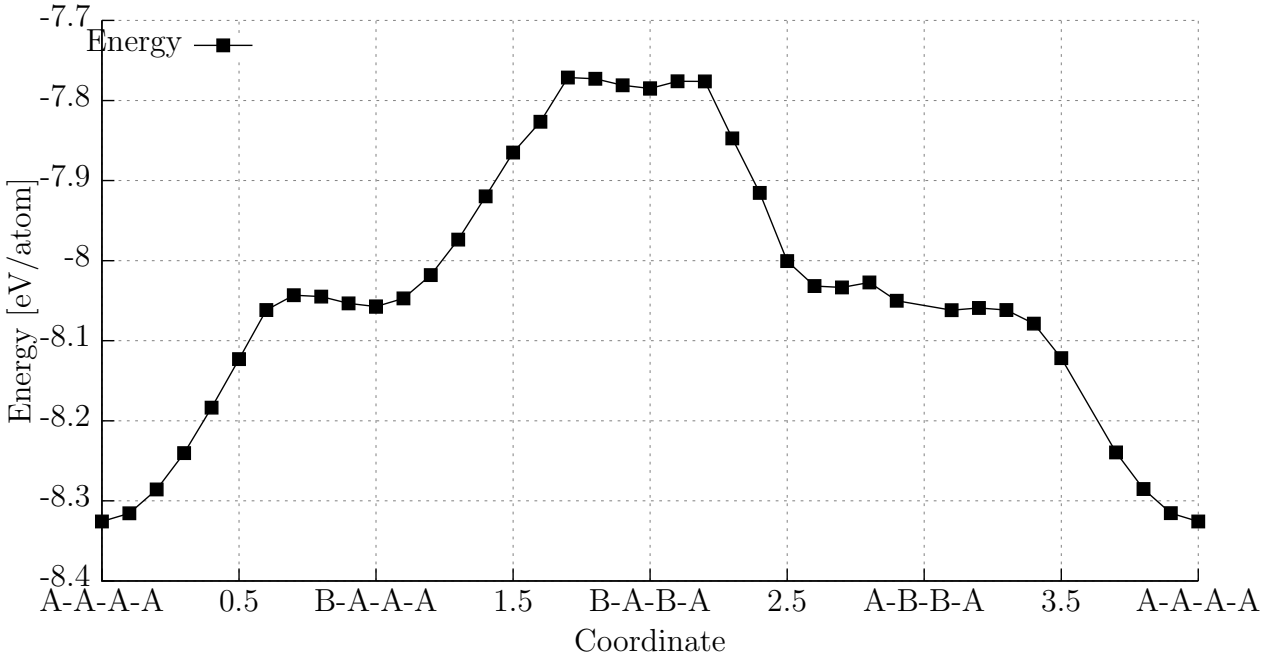

Figure 2.13: Total energy landscape for ZrB_2.

In summary, we have found various local energy minima at different stackings. The next step is to evaluate if these local minima correlate to a metastable structure. The smaller the energy barrier between two different stackings, the easier it is to create stacking faults and therefore a transformation from one stacking to the next one can procees. Many of these energy barriers are small (0.2–0.3 eV/at.) between the B-A-B-A and the A-B-B-A stacking, which means that only small inputs are needed to change the stacking sequence. This evaluation is done in Sec. 2.4 via a phonon analysis.

2.3 Shearing of Planes by Tilting

In contrast to the previous section, where shear was applied to only one plane, we now investigate energy barriers when homogeneous shear is applied.We start from an A-A-A-A stacking and tilt the c-axis of the crystal in three different directions according to the following specification: $c' = c + ka$, $c' = c + k(a + b)$, $c' = c + k(a - b)$, further called the a-direction, the $a + b$-direction and the $a - b$-direction. It means that the $\vec{c}$ lattice vector is tilted in $\vec{a}$, $\vec{a} + \vec{b}$ or $\vec{a} - \vec{b}$ direction. Parameter k describes the magnitude of the tilt; $k = 1$ means that we a lattice translational vector is added and hence the A-A-A-A stacking is again recovered.

We notice that the results for the tilting in the a-direction is equal to the tilting in the $a + b$-direction, which results from the crystallographic equivalence of these planes. The few points they differ are caused by the boron atoms getting stuck between the metal atoms and therefore being unable to relax into a lower energy state.

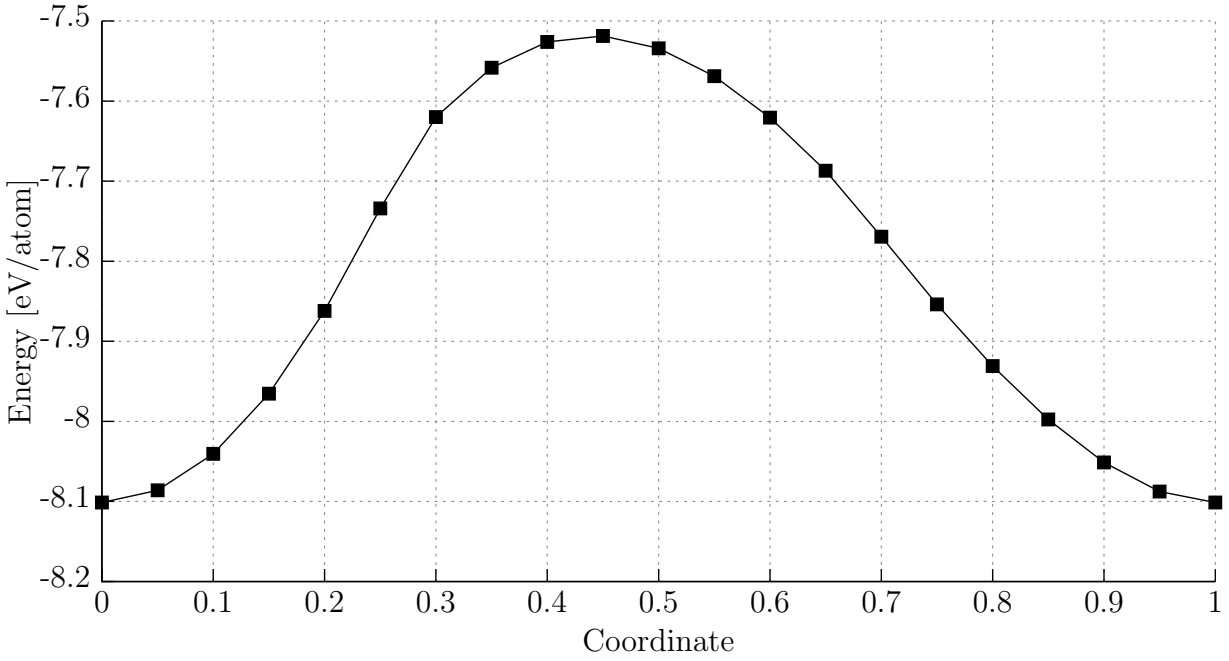

Figure 2.14: Shearing of TiB_2 in the a-direction.

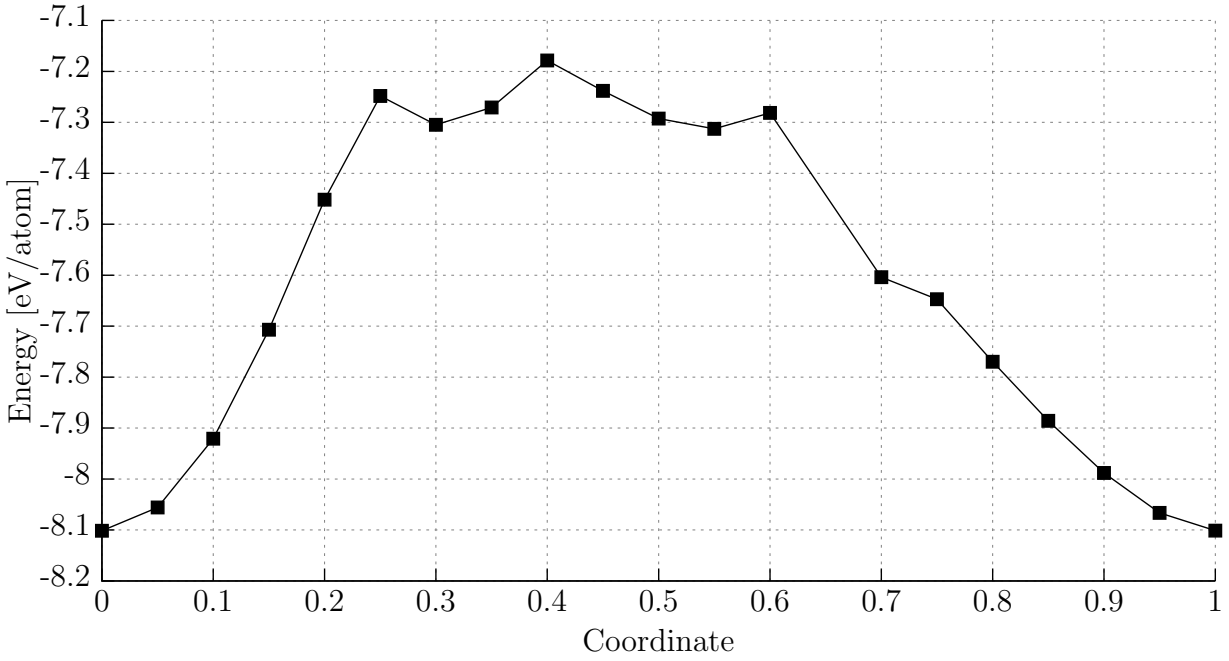

Figure 2.15: Shearing of TiB_2 in the $a - b$-direction.

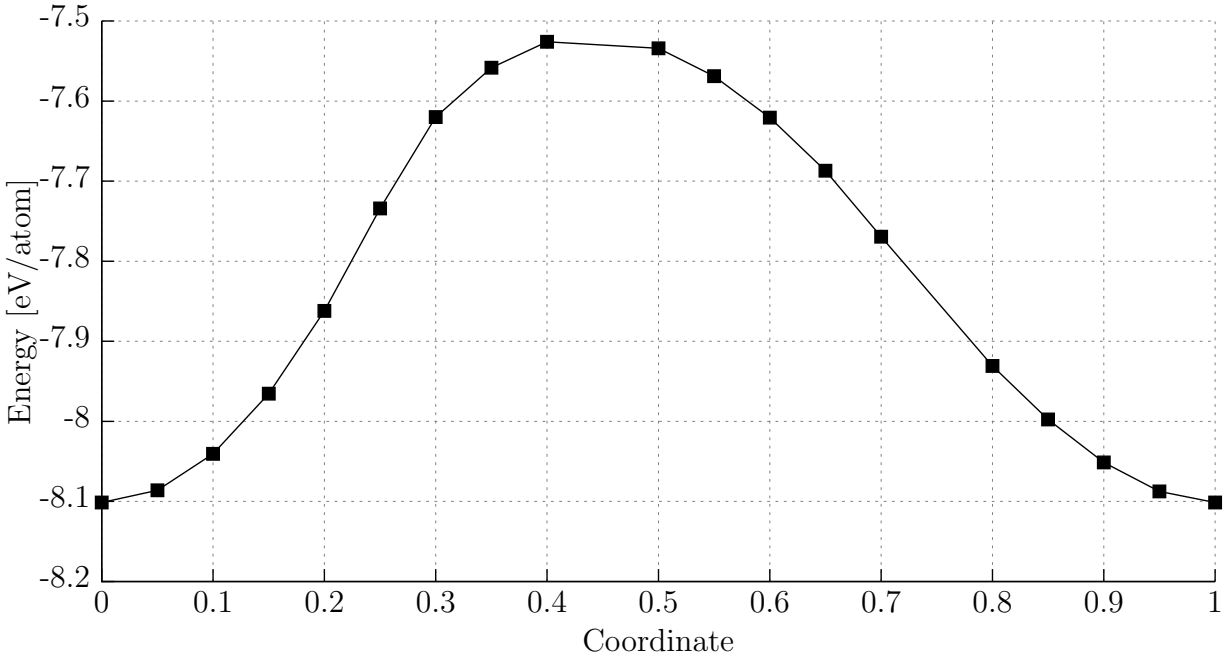

Figure 2.16: Shearing of TiB_2 in the $a + b$-direction.

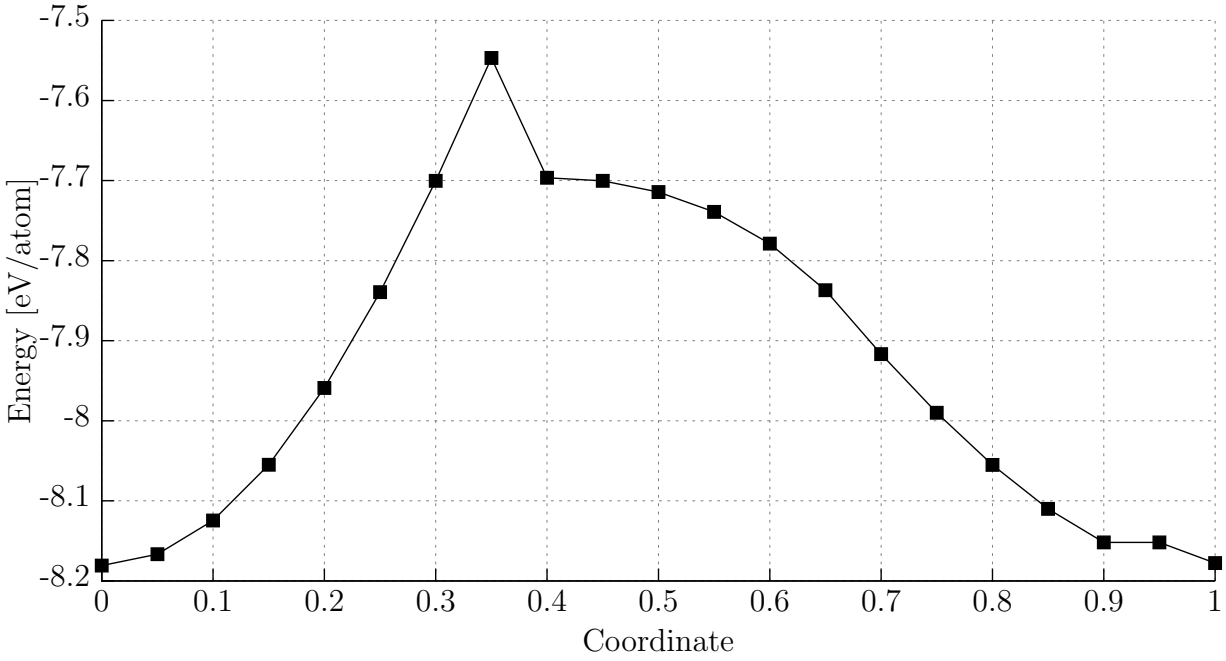

Figure 2.17: Shearing of VB_2 in the a-direction.

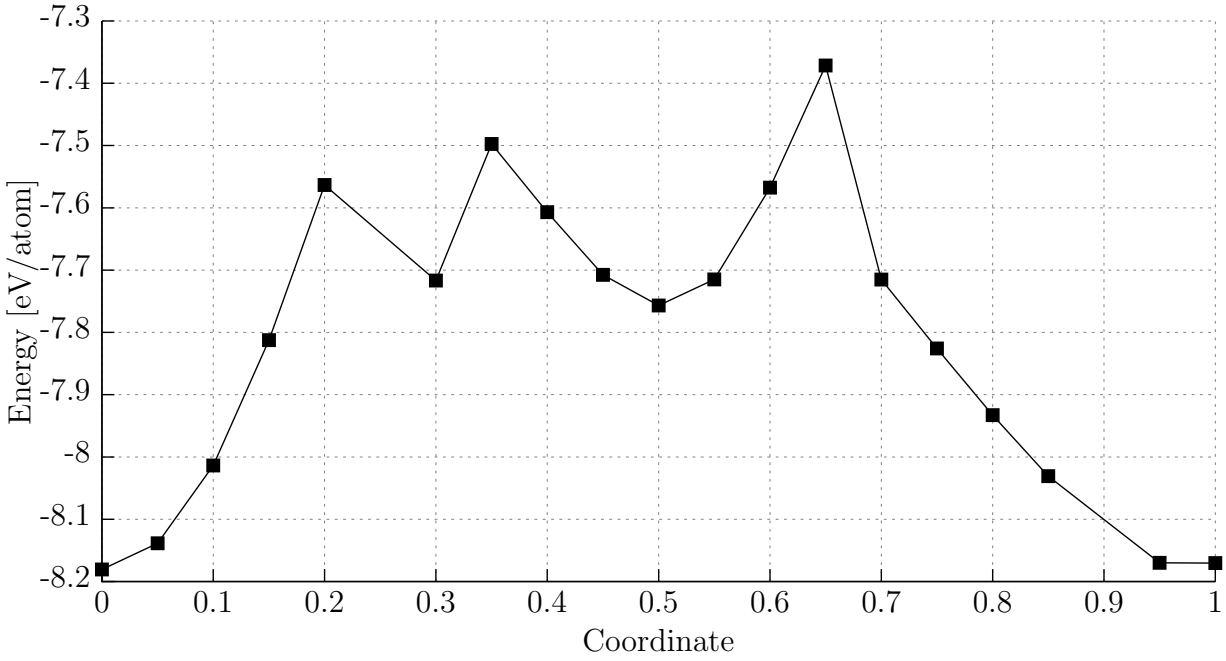

Figure 2.18: Shearing of VB_2 in the $a - b$-direction.

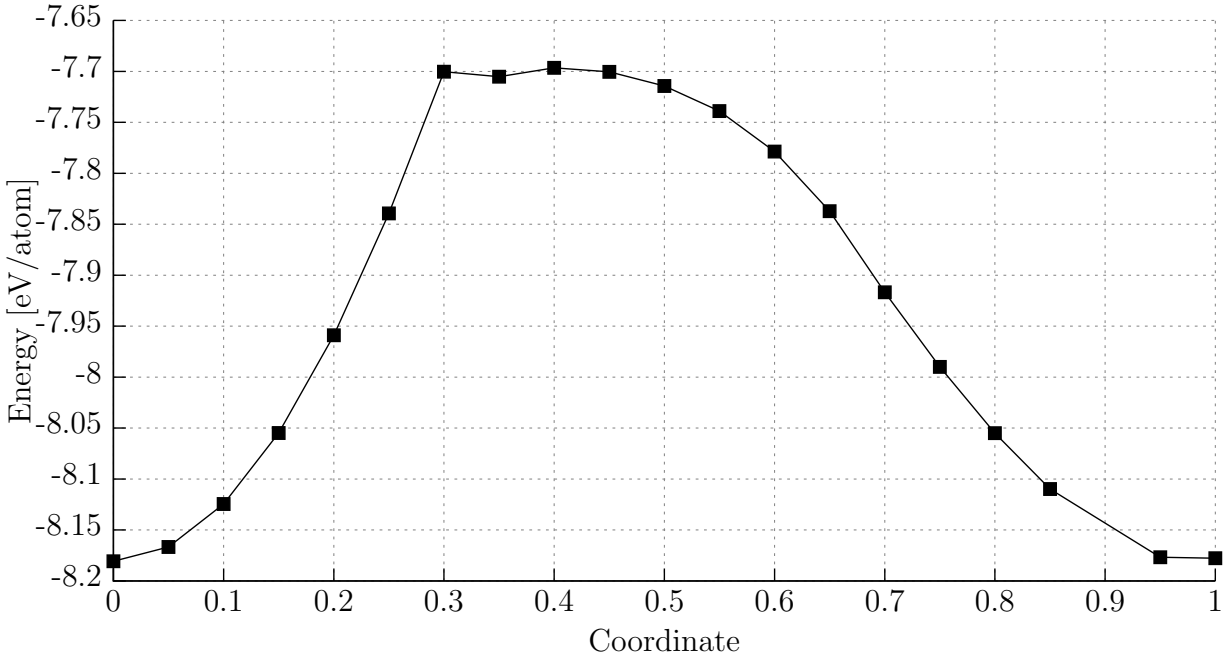

Figure 2.19: Shearing of VB_2 in the $a + b$-direction.

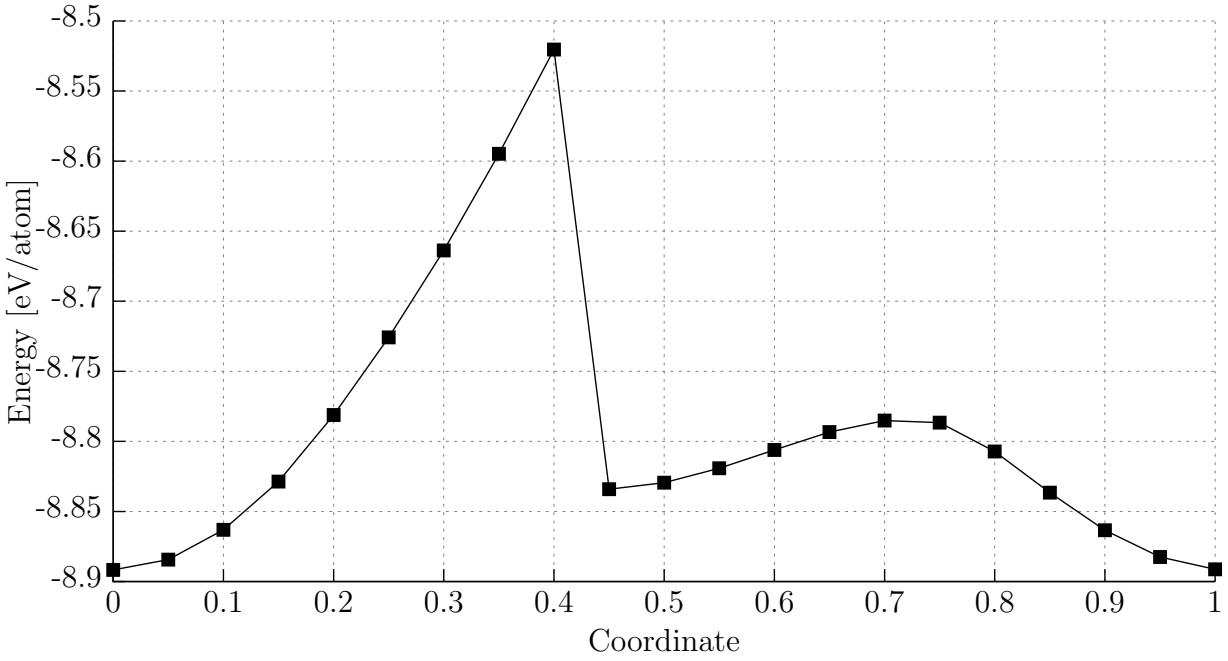

Figure 2.20: Shearing of WB_2 in the a-direction.

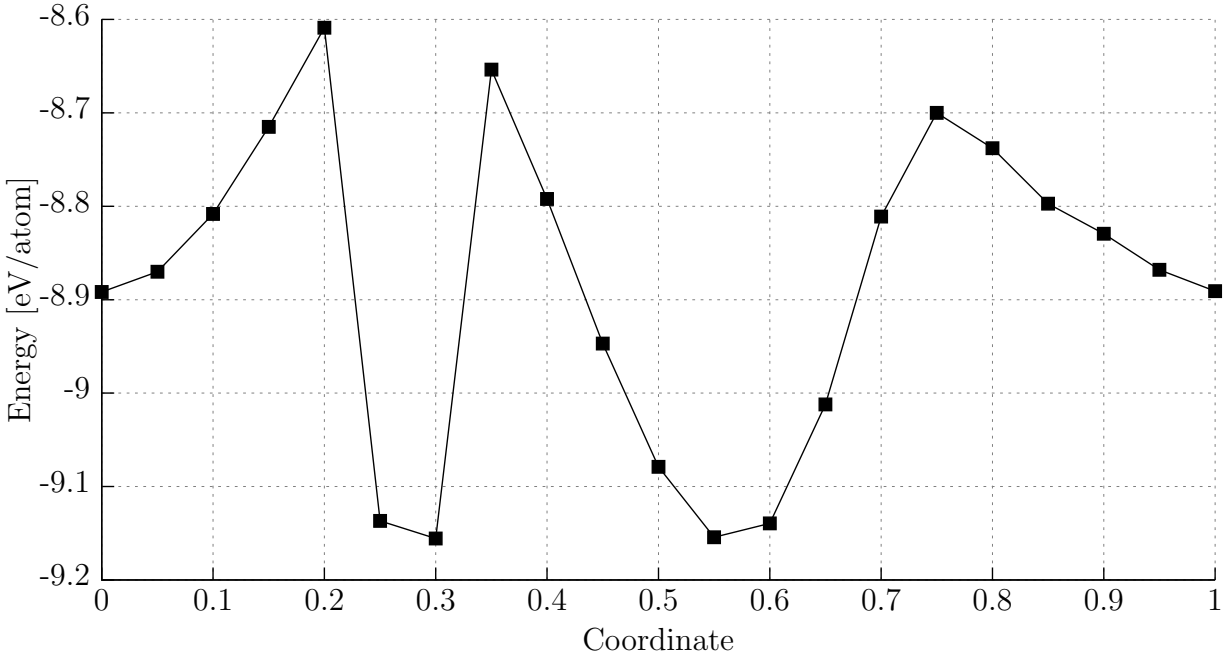

Figure 2.21: Shearing of WB_2 in the $a - b$-direction.

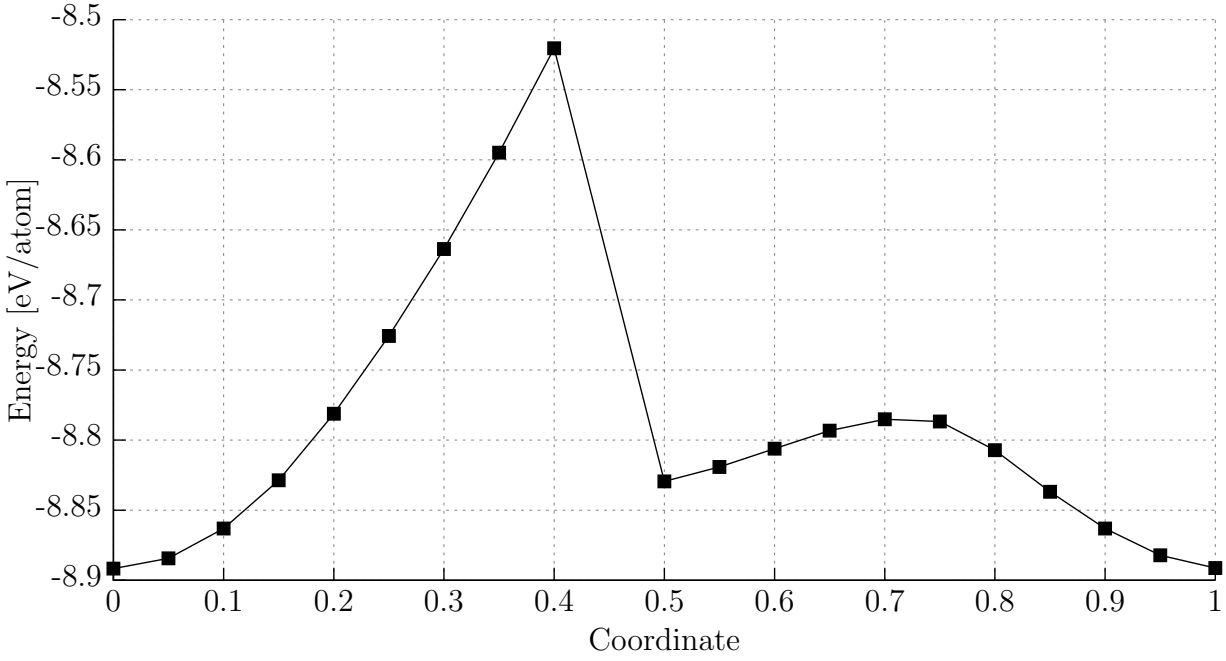

Figure 2.22: Shearing of WB_2 in the $a + b$-direction.

When tilting TiB_2 in the a-direction, we get a smooth curve which reflects the tendency of the boron atoms to find a lower energy state in the A-A-A-A stacking. When tilting the c-axis in the $a-b$-direction, the total energy has local minima at the 0.3 and 0.55 coordinate related to the boron electrons moving and relaxing into a metastable state.

VB_2 shows similar behaviour as TiB_2; when tilted into the $a-b$-direction, the local minima are even more pronounced than in the case of TiB_2.

Lastly, the A-A-A-A-stacked WB_2 transforms to a lower energy states when tilted in the $a-b$-direction. This suggests a stable structure with a lower energy state and different stacking than the A-A-A-A stacking.

2.4 Analysis of Dynamical Stability with Phonopy

It is of a particular interest to find out, if each of the identified local energy minima represents a stable or unstable structure. One way to investigate that is to analyse their phonon density of states (DOS) and their phonon frequencies. A dynamically stable structure contains only phonon modes corresponding to positive frequencies, whereas negative values (or, more precisely, imaginary frequencies) signify dynamically unstable structures.

CrB_2

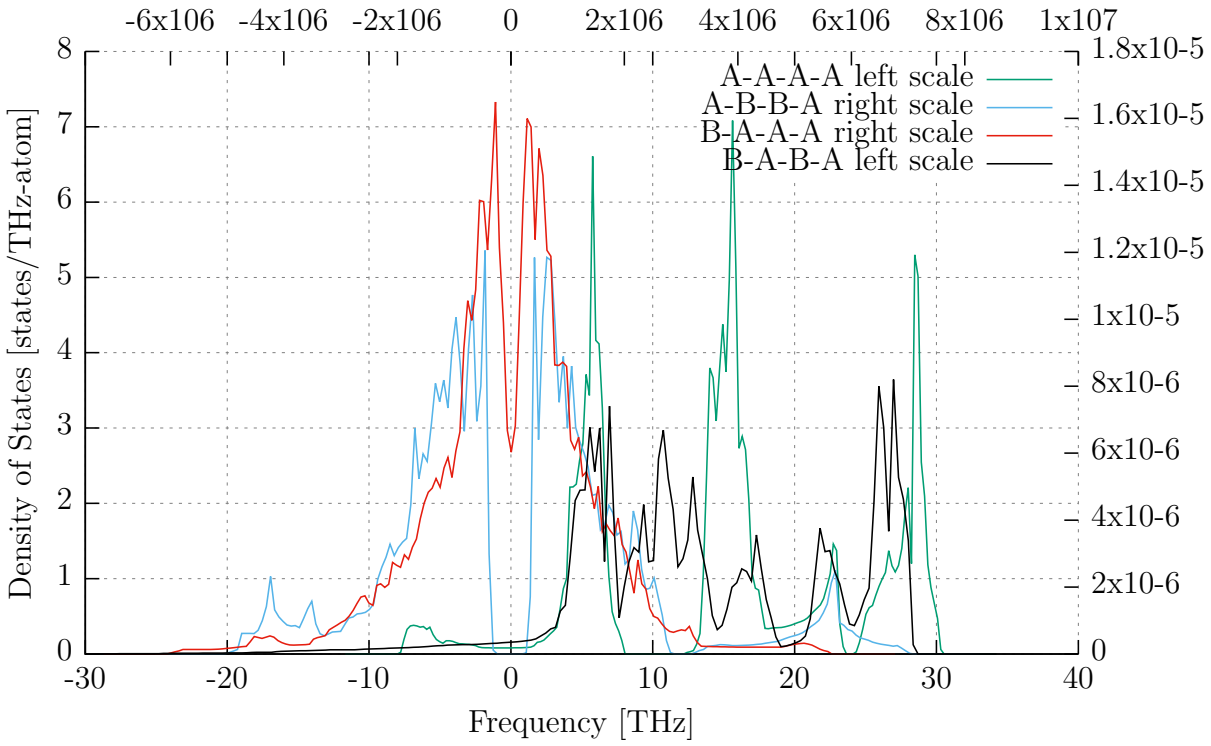

Figure 2.23: Phonon DOS of different CrB_2 stackings.

What we see in Fig. 2.23 for CrB_2 is a recurring pattern for many other MeB_2. Because of their non-zero values for the DOS at negative frequencies, we conclude that the A-B-B-A and the B-A-A-A stackings are unstable configurations for CrB_2. The A-A-A-A and the B-A-B-A stacking show only little values for the negative (imaginary) frequencies which may be related to numerical inaccuracies. Those structures are likely to be stable but should be tested more closely for their stability.

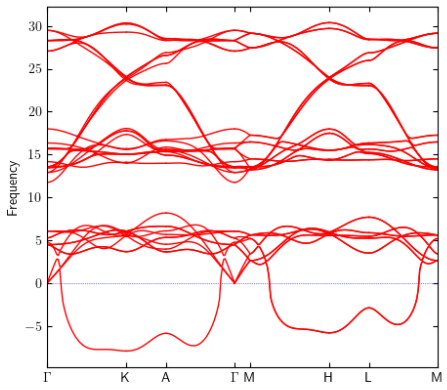

Figure 2.24: Phonon dispersion of the A-A-A-A-stacked CrB_2.

As we can see in Fig. 2.24, there is only one phonon mode which shows negative frequencies. Unlike that, the B-A-B-A stacking exhibits many modes with imaginary frequencies (Fig. 2.25), related to the high phonon DOS (Fig. 2.23) for negative frequencies, and hence is indeed unstable.

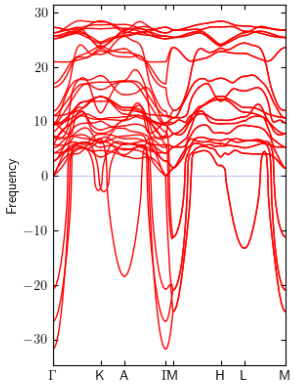

Figure 2.25: Phonon dispersion of B-A-B-A CrB_2

Figure 2.26 visualises the displacements for the negative phonon mode in Fig. 2.24 at the Γ point. The displacements suggest that the structure might not be in a fully relaxed state,

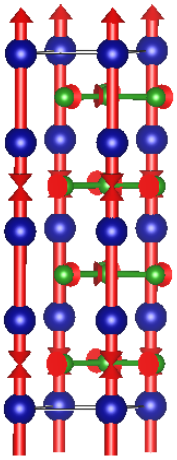

Figure 2.26: Displacements of atoms for A-A-A-A stacking of CrB_2 corresponding to the most negative frequency.

where planes of metal still atoms want to shift along the z-direction with simultaneous shift of the B planes in-plane. We can conclude therefore that the A-A-A-A stacking is the most likely stable structure for CrB_2. We note, that these slight instabilities may be also related to the neglection of magnetic interactions, as our calculations did not include any spin-polarisation.

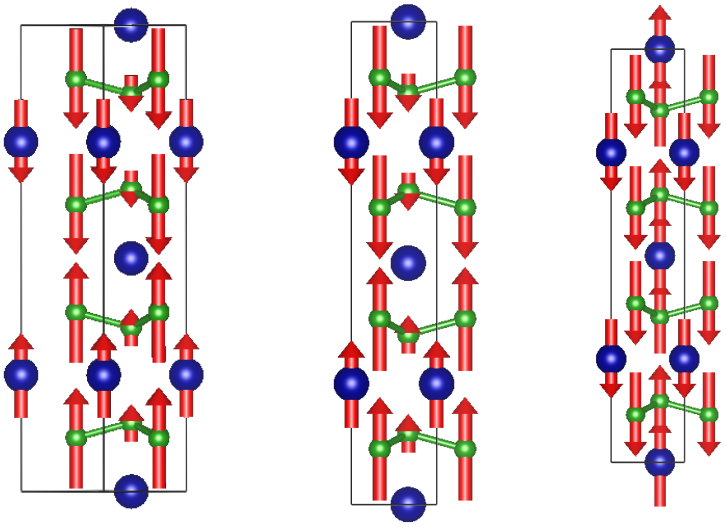

Figure 2.27: Displacements of the atoms for B-A-B-A CrB_2 for 3 modes with the most negative frequencies at the Γ point.

Taking a look at the imaginary-frequency phonon modes of the B-A-B-A stacking (Fig. 2.25) and the corresponding displacements on the atoms (Fig. 2.27) at Γ-point, we can come to no simple solution for a mechanism to stabilise this structure.

HfB_2

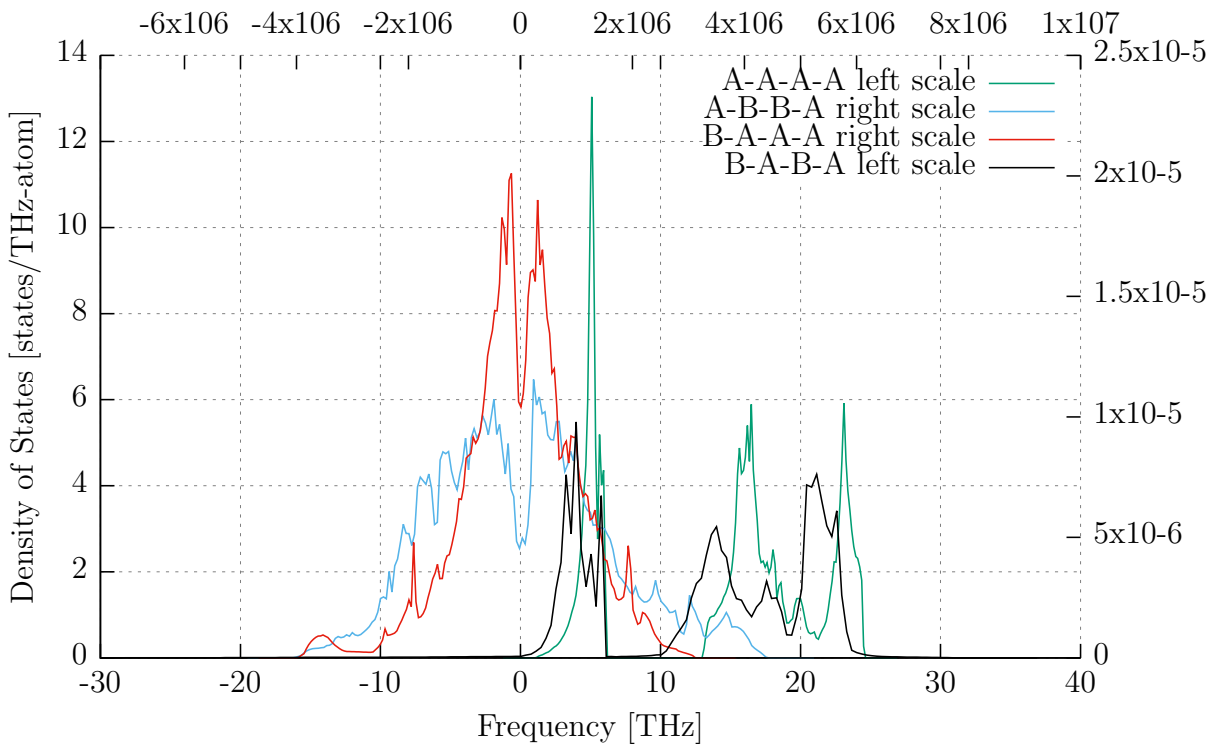

Figure 2.28: Phonon DOS of different HfB_2 stackings.

Figure 2.28 shows that no DOS at negative (imaginary) frequencies for the A-A-A-A stacking and only a small one for the B-A-B-A stacking. The A-B-B-A and B-A-A-A stackings can be dismissed as unstable structures.

Phonon dispersion in Fig. 2.29 shows no negative phonon frequencies, hence we can conclude that the A-A-A-A stacking is a stable structure.

As seen in Fig. 2.30, for the B-A-B-A stacking, HfB_2 shows two negative phonon frequencies at the Γ point. Fig. 2.31 shows the atomic displacements at the Γ point for the two negative phonon frequencies.

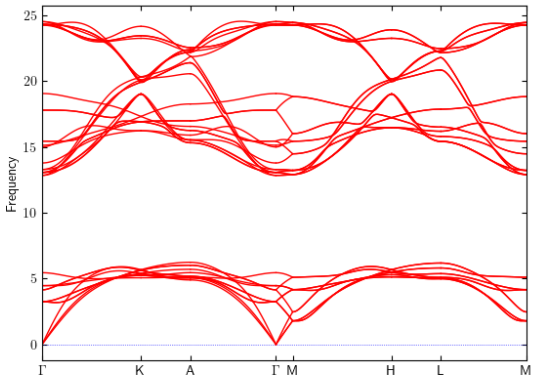

Figure 2.29: Phonon dispersion of the A-A-A-A-stacked HfB_2.

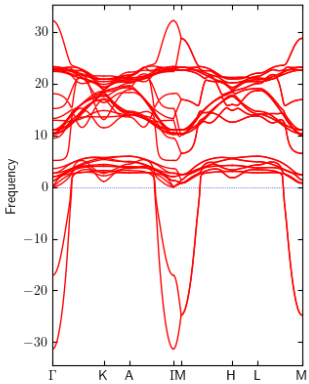

Figure 2.30: Phonon dispersion of the B-A-B-A-stacked HfB_2.

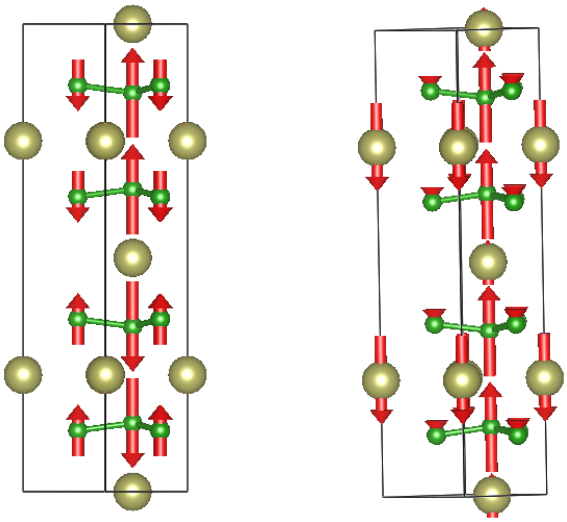

Figure 2.31: Atomic displacements corresponding to the 2 imaginary frequencies at the Γ point of the B-A-B-A stacking of HfB_2.

MnB_2

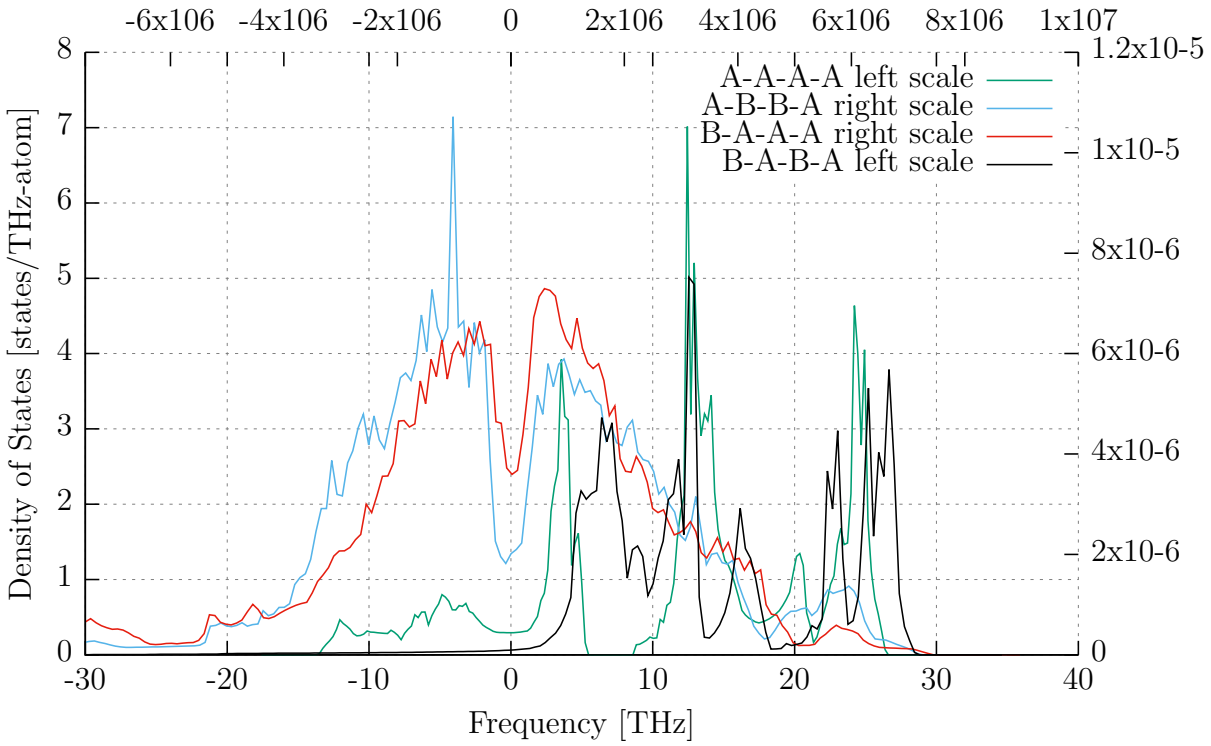

Figure 2.32: Phonon DOS of different stackings of MnB_2.

In Fig. 2.32 we see almost no phonon DOS at negative frequencies for the B-A-B-A stacking. Non-negligible phonon DOS at imaginary frequencies is predicted for the A-A-A-A stacking. The A-B-B-A and B-A-A-A stackings can be dismissed as unstable structures.

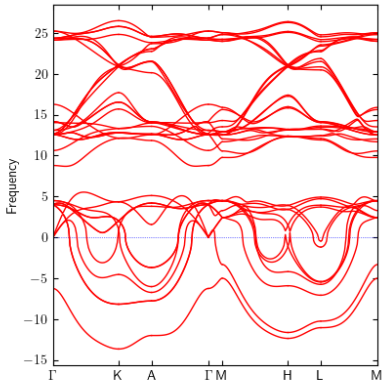

Figure 2.33: Phonon dispersion of the A-A-A-A stacked MnB_2.

Fig. 2.34 shows the forces on the atoms for the A-A-A-A stacking of MnB_2 at the Γ point (Fig. 2.33). It leads to the conclusion that the MnB_2 is not fully relaxed along the *c*-direction,

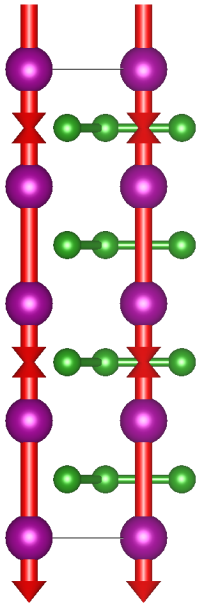

Figure 2.34: Atomic displacements for the A-A-A-A stacking of MnB_2.

which can be again related to the symmetry-forbidden relaxation at 0 K, similarly to CrB_2. It may be therefore possible to obtain a stable structure for the A-A-A-A-stacked MnB_2.

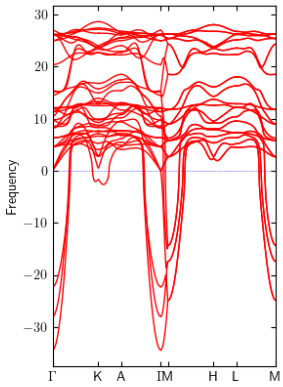

Figure 2.35: Phonon dispersion of the B-A-B-A-stacked MnB_2.

Interestingly, also the B-A-B-A-stacked MnB_2 exhibits imaginary phonon modes (Fig. 2.35), suggesting that also in this configuration our structure is not perfectly relaxed.

MoB_2

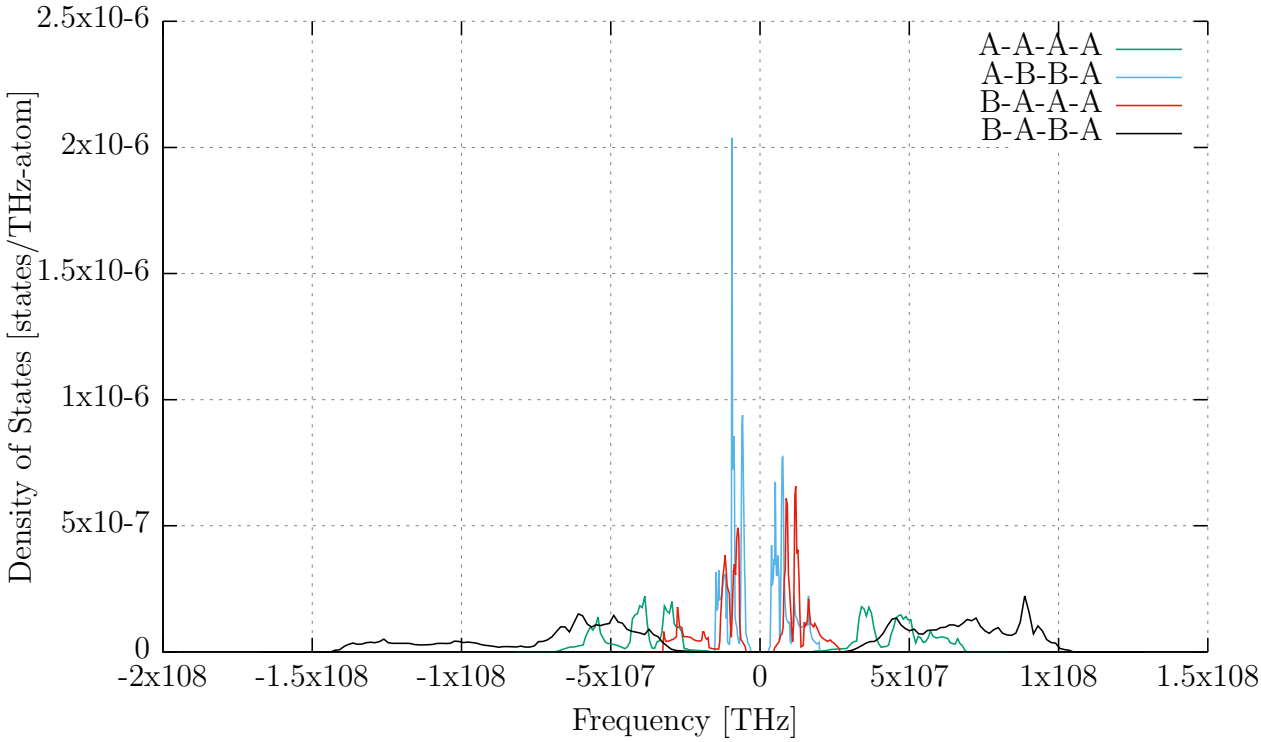

Figure 2.36: Phonon DOS of different MoB_2 stackings.

As seen in Fig. 2.36 for MoB_2 there seems to be no stable structure in the observed stackings. This might be due to Mo forming a stable structure with B as Mo_2B_5. Similarly, our structures may not be ideally relaxed, as already discussed above for other MeB_2. Apart from the A-A-A-A stacking, which corresponds to the local minimum on the energy landscape (Fig. 2.6), all other structures have local minima "nearby" along the transformation path, hence correlating with the phonon instability.

NbB_2

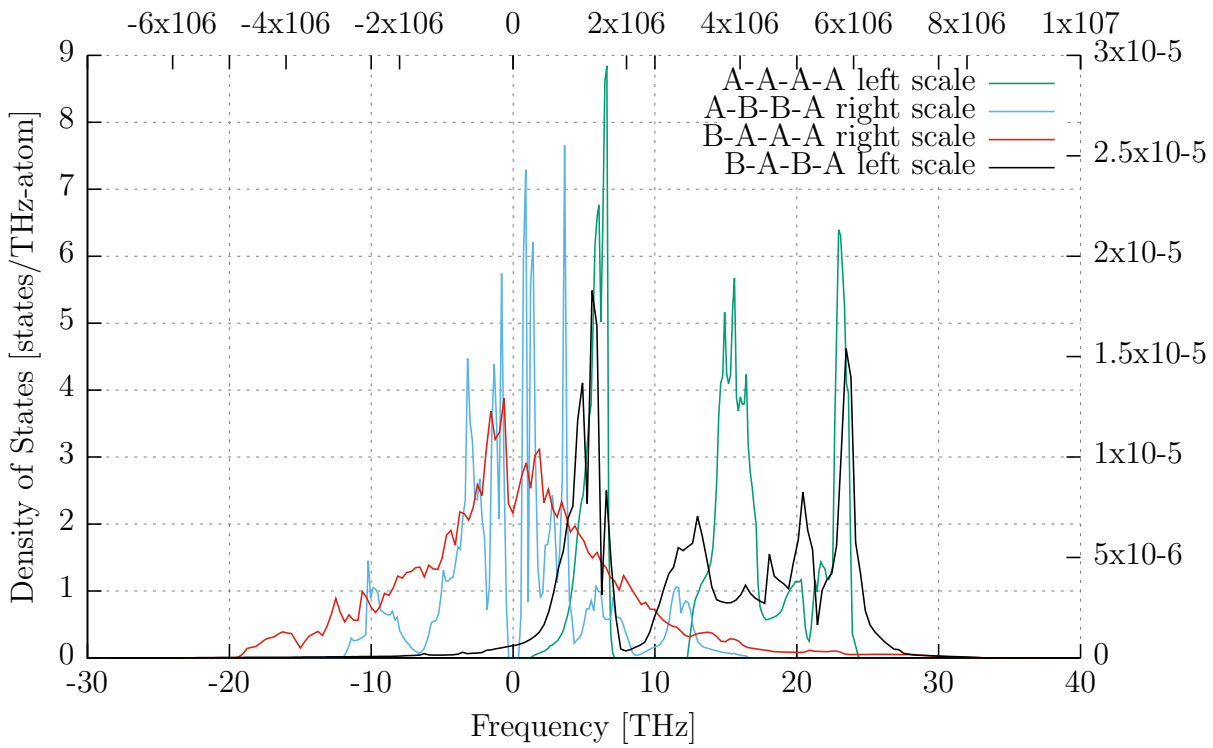

Figure 2.37: Phonon DOS of different NbB_2 stackings.

The same behaviour as for HfB_2 is predicted also for NbB_2. The A-A-A-A is the stable stacking (Fig. 2.38) and the B-A-B-A stacking might be stabilised (Fig. 2.39).

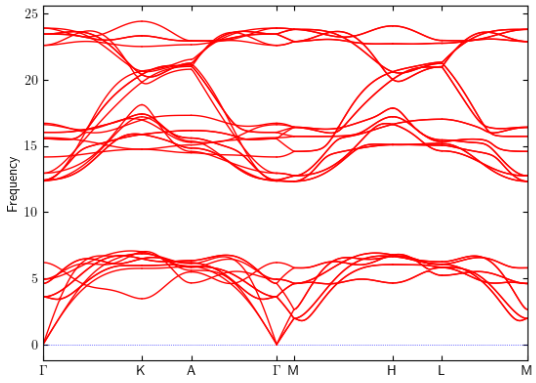

Figure 2.38: Phonon dispersion of the A-A-A-A stacking of NbB_2.

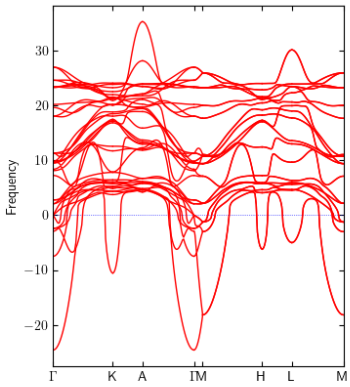

Figure 2.39: Phonon dispersion of the B-A-B-A stacking of NbB_2.

ReB_2

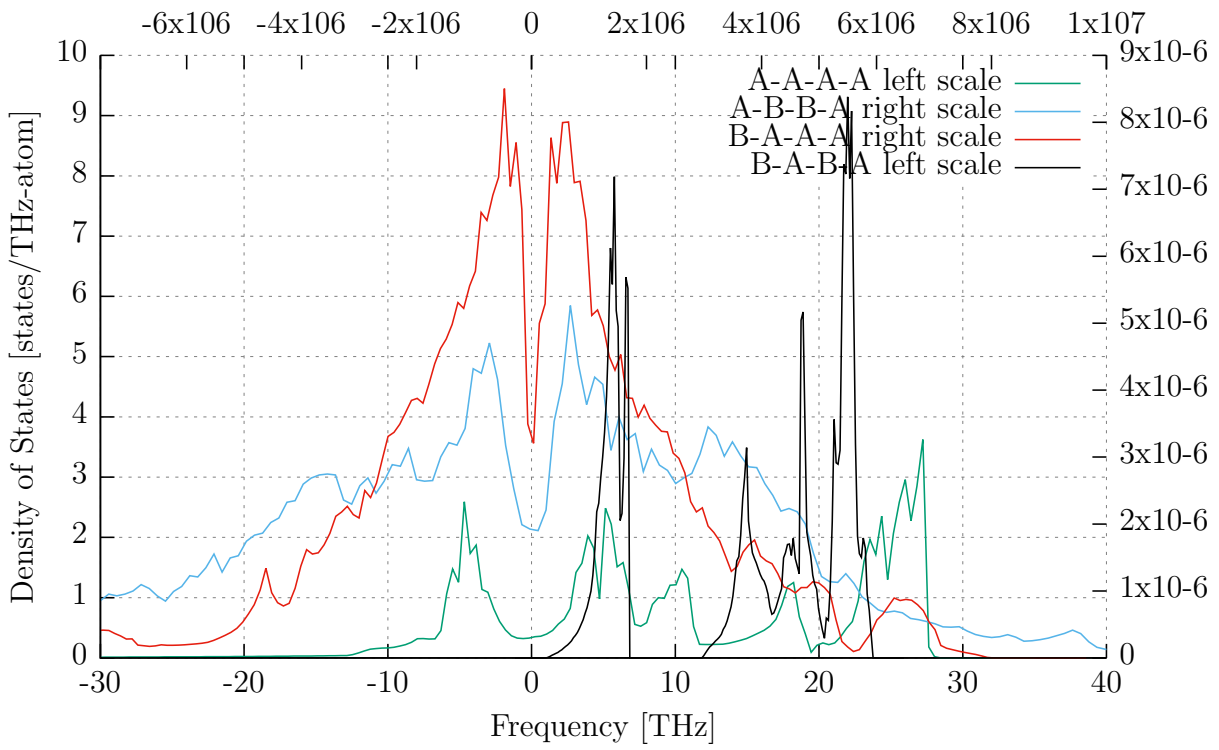

Figure 2.40: Phonon DOS of different ReB_2 stackings.

ReB_2 behaves oppositely to most of the other MeB_2 we have discussed so far, and it is similar to MnB_2. Here, the B-A-B-A structure is fully stable (Fig. 2.41) and the A-A-A-A structure is the one which might be stabilised (Fig. 2.42).

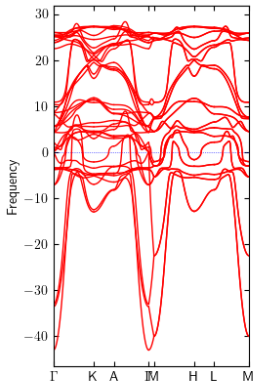

Figure 2.41: Phonon dispersion of the A-A-A-A-stacked ReB_2.

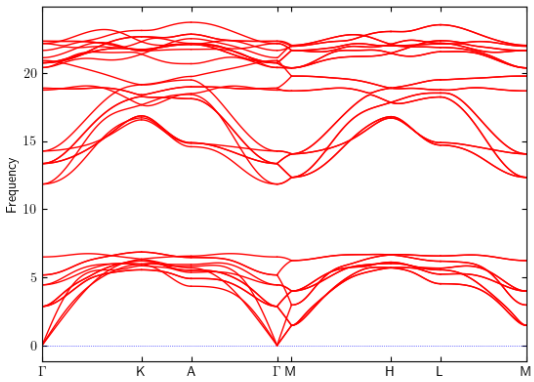

Figure 2.42: Phonon dispersion of B-A-B-A-stacked ReB_2.

TaB_2

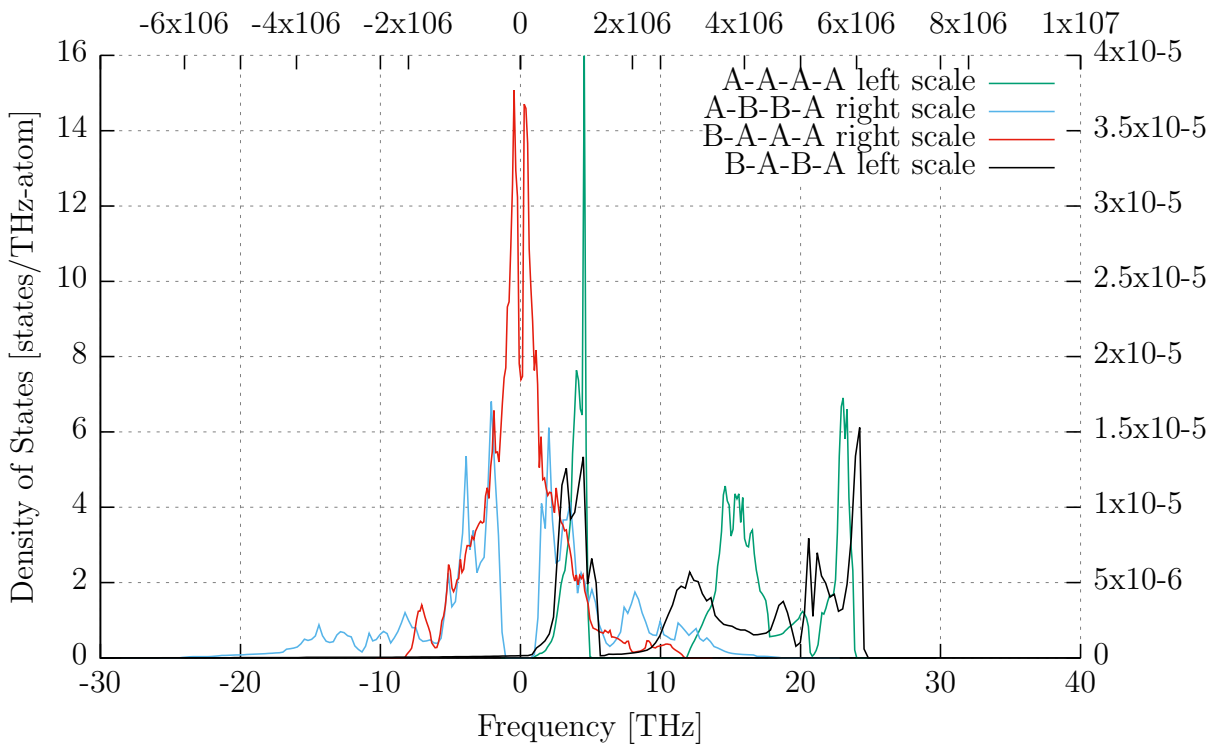

Figure 2.43: Phonon DOS of different TaB_2 stackings.

For TaB_2, the same conclusions as for HfB_2 apply.

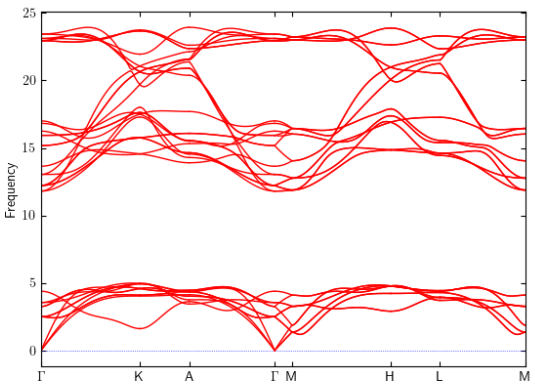

Figure 2.44: Phonon dispersion of A-A-A-A-stacked TaB_2.

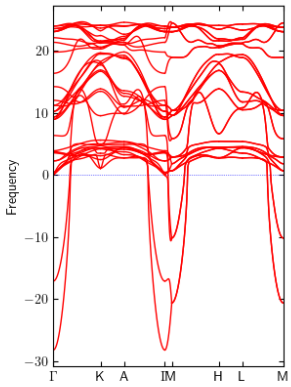

Figure 2.45: Phonon dispersion of B-A-B-A-stacked TaB_2.

TiB_2

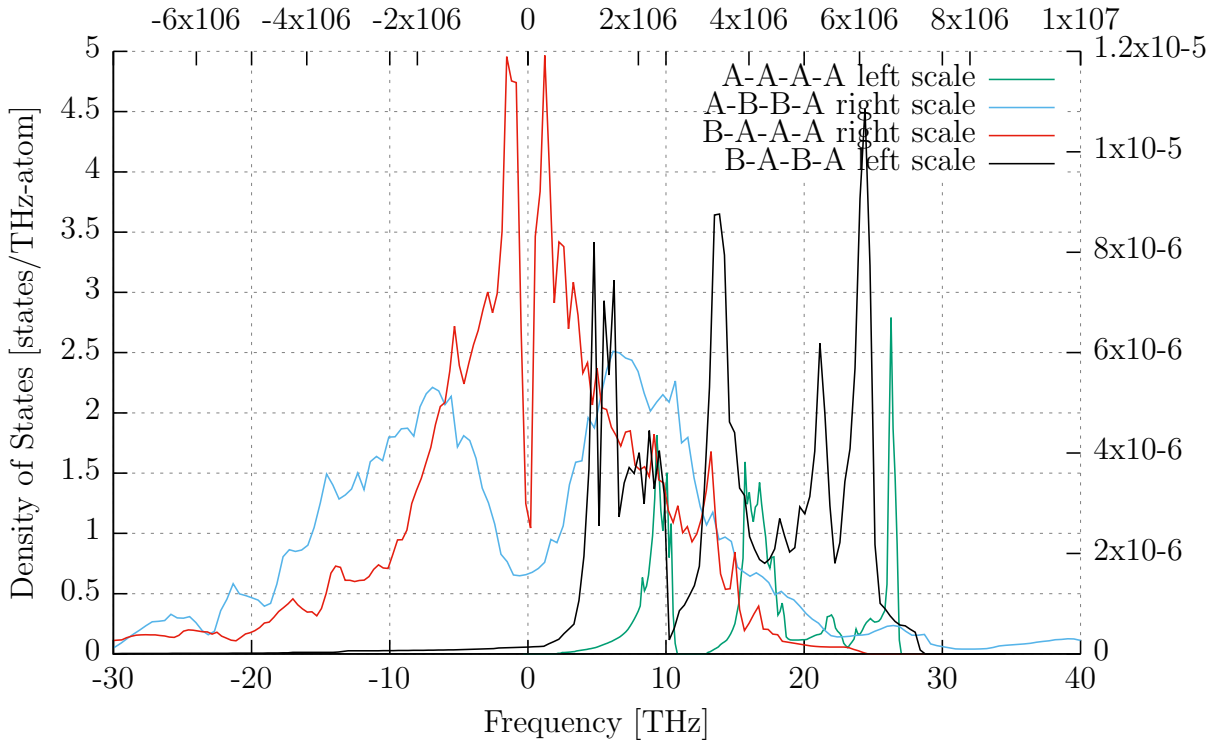

Figure 2.46: Phonon DOS of different TiB_2 stackings.

For TiB_2, the same conclusions as for HfB_2 apply.

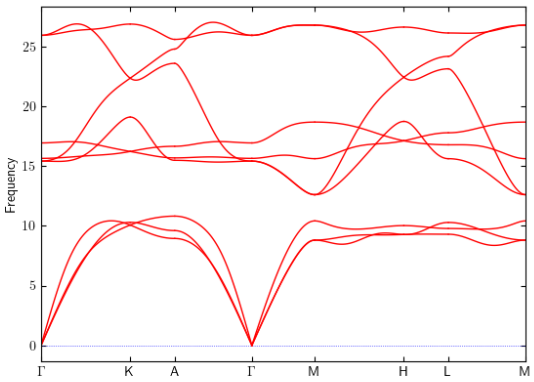

Figure 2.47: Phonon dispersion of A-A-A-A-stacked TiB_2.

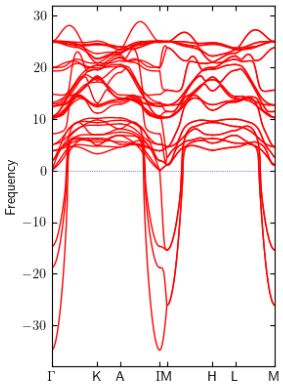

Figure 2.48: Phonon dispersion of B-A-B-A-stacked TiB_2.

VB_2

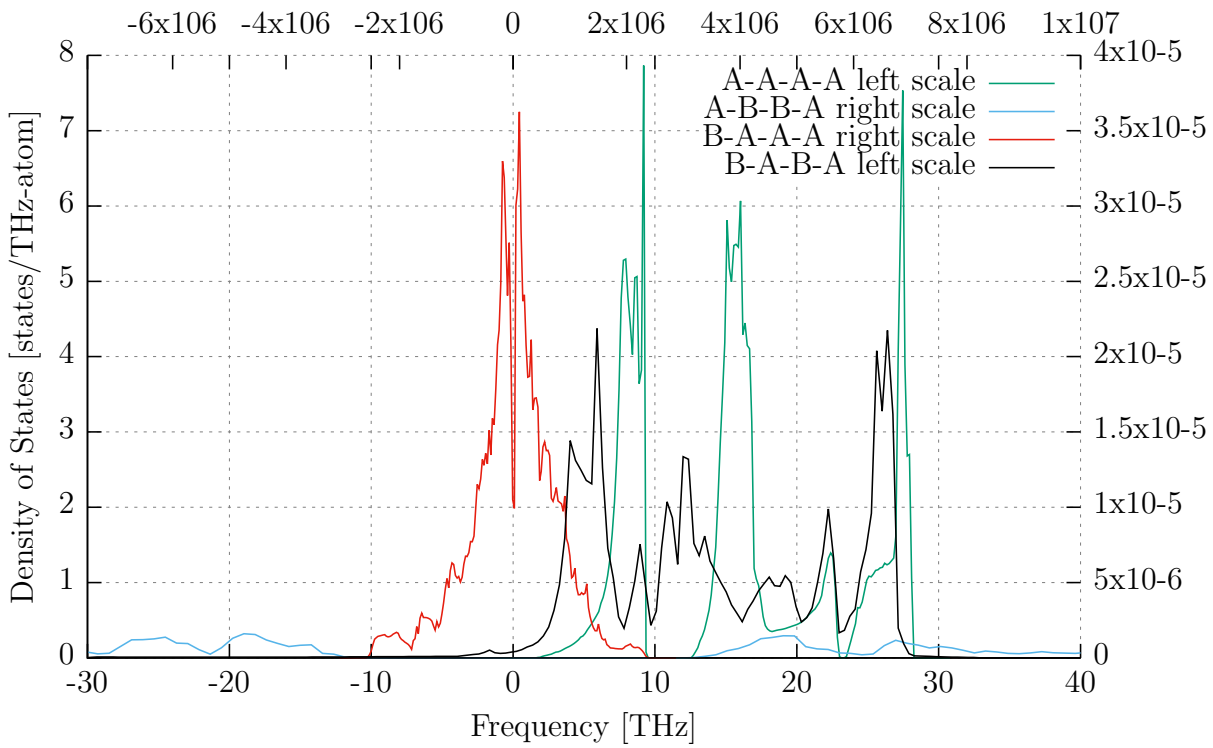

Figure 2.49: Phonon DOS of different VB_2 stackings.

For VB_2, the same conclusions as for HfB_2 apply.

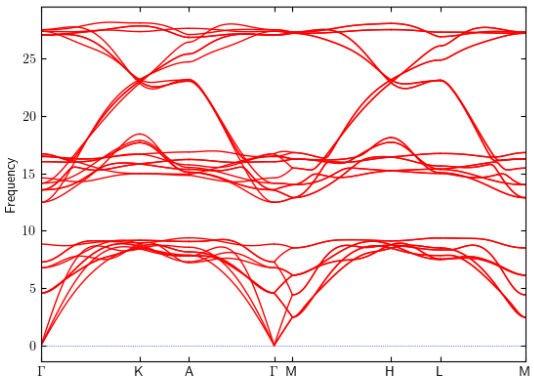

Figure 2.50: Phonon dispersion of A-A-A-A-stacked VB_2.

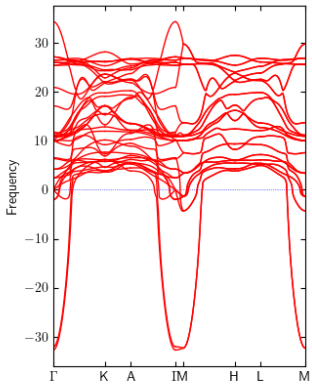

Figure 2.51: Phonon dispersion of B-A-B-A-stacked VB_2.

WB_2

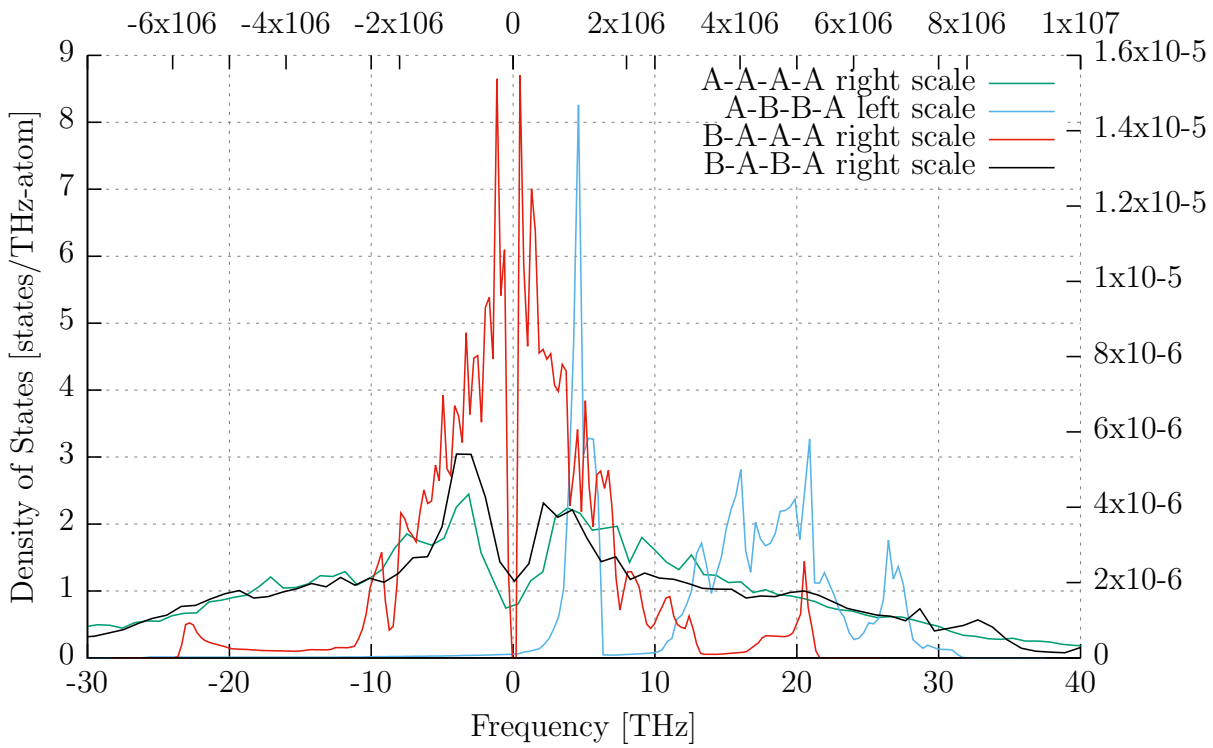

Figure 2.52: Phonon DOS of differently stacked WB_2 structures.

As seen in Fig. 2.52, WB_2 has its stable structure at the A-B-B-A stacking while the other structures are clearly unstable. Nevertheless, the phonon dispersion of the A-B-B-A stacking in Fig. 2.54 reveals that some phonon modes still exhibit imaginary phonon frequencies, and hence our structural model is not yet fully relaxed. Similarly to MoB_2, instability may be related also to the fact, that slightly off-stoichiometric compositions W_2B_{5-x} are preferred.

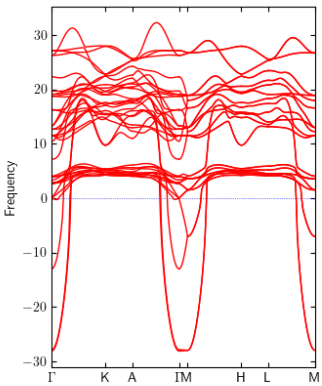

Figure 2.53: Phonon dispersion of A-B-B-A-stacked WB_2.

ZrB_2

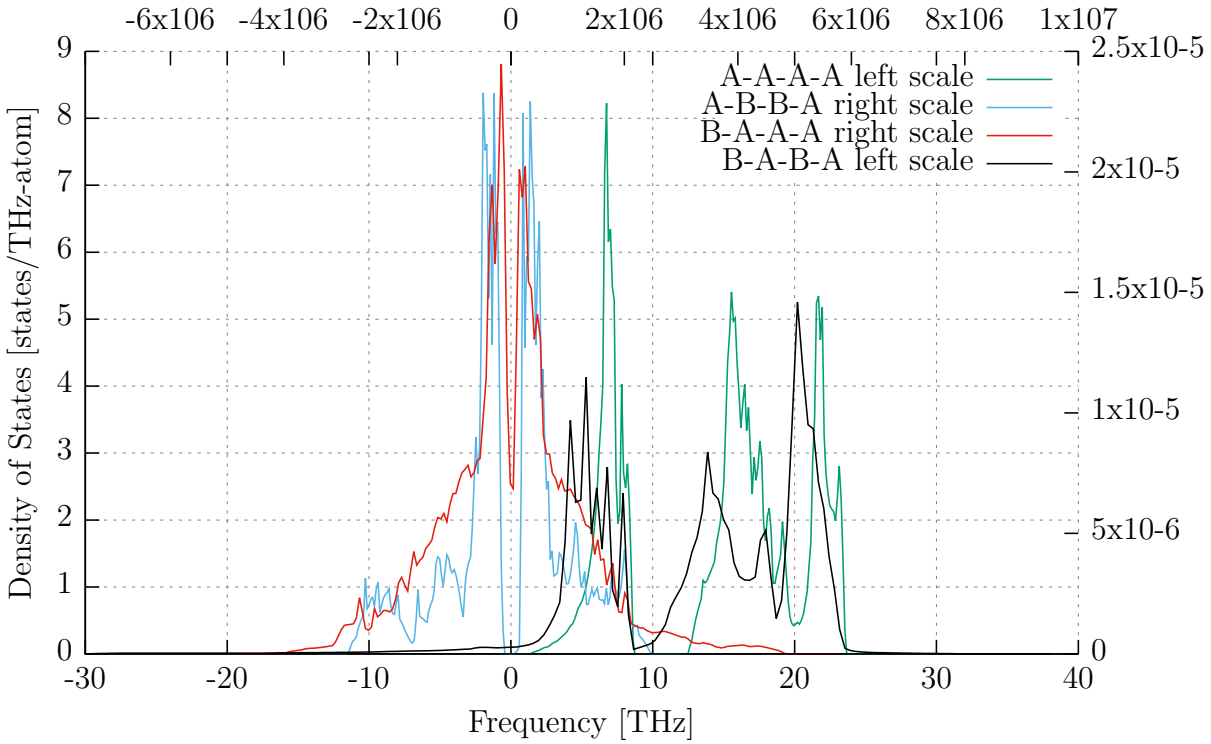

Figure 2.54: Phonon DOS of different stackings of ZrB_2.

For ZrB_2, the same conclusions as for HfB_2 apply.

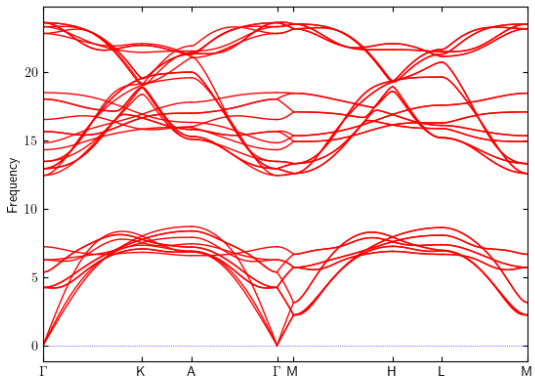

Figure 2.55: Phonon dispersion of the A-A-A-A-stacked ZrB_2.

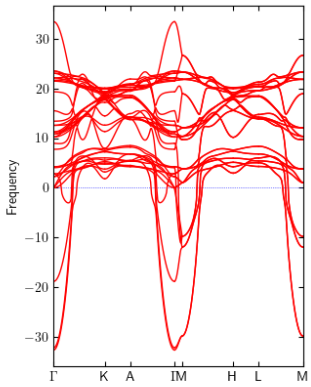

Figure 2.56: Phonon dispersion of the B-A-B-A-stacked ZrB_2.

Conclusions from the Dynamical Stability

No negative phonon frequencies are obtained only for the known stable structures. Structures with only a few soft phonon modes may be stabilized by a careful structural optimisation. This is predicted for the B-A-B-A structures for MeB_2 with the stable A-A-A-A stacking, but never in the B-A-A-A stacking and the A-B-B-A stacking. None of these structures is stable for MoB_2. WB_2 is only stable in the A-B-B-A stacking and ReB_2 in the B-A-B-A structure, with a possible stability in the A-A-A-A stacking.

Chapter 3

Summary and Outlook

The energy landscapes (Sec. 2.2) helped us identifying local energy minima, while the analysis with dynamical stability (Sec. 2.4) enabled us to take a closer look to discern which of these local energy minima might result in a stable or metastable structure.

The stable stacking sequence for the MeB_2 (Me=Cr, Hf, Mn, Nb, Ta, Ti, V, Zr) was identified as the α-structure (A-A-A-A stacking), except for ReB_2 and WB_2, where the stable stacking orders were B-A-B-A and A-B-B-A, respectively. No stable structure for MoB_2 was found in this investigation.

The phonon analysis suggests possible metastable structures for the above mentioned MeB_2 in the B-A-B-A stacking and ReB_2 in the A-A-A-A stacking, but the energy barriers between those stackings and other, metastable/unstable stackings, were identified to be very small. Therefore, stabilising structures with these stackings might be difficult. A way to stabilise those structures was not identified in this work and is subject to further investigations.

Bibliography

[1] G. Qin, Q. Cui, A. Du, W. Wang, and Q. Sun, ChemCatChem **11**, 2624 (2019).

[2] H. Yuan, Z. Li, and J. Yang, J. Phys. Chem. C **123**, 16294 (2019).

[3] B. Basu, G. B. Raju, and A. K. Suri, Int. Mater. Rev. **51**, 352 (2006).

[4] M. Matkovich, G. Samsonov, P. Hagenmuller, and T. Lundstrom, *Boron and refractory borides* (Springer, Berlin, Heidelberg, 1977).

[5] "What to Know About Harvey Tool's TiB2 Coating," `https://www.harveyperformance.com/in-the-loupe/tib2-coating/`, accessed: 2021-05-09.

[6] L. A. F. Peçanha Jr, S. N. Monteiro, Í. do Vale Tomaz, M. M. de Oliveira, A. M. Ramalho, N. T. Simonassi, and F. de Oliveira Braga, J. Mater. Res. Technol **7**, 550 (2018).

[7] J. Shappirio, J. Finnegan, R. Lux, D. Fox, J. Kwiatkowski, H. Kattelus, and M.-A. Nicolet, J. Vac. Sci. Technol **3**, 2255 (1985).

[8] R. M. Santos da Silva Cruz, *TiB_2 ceramic and DLC Multilayered PVD coatings*, Ph.D. thesis, Cranfield University (2007).

[9] W. Herr, G. Berg, C. Friedrich, E. Broszeit, and K. Kloos, Materialwissenschaft und Werkstofftechnik **25**, 175 (1994).

[10] R. Savino, S. Mungiguerra, and G. Di Martino, Adv. Appl. Ceram. **117**, s9 (2018).

[11] P. Lespade, N. Richet, and P. Goursat, Acta Astronaut. **60**, 858 (2007).

[12] J. Nagamatsu, N. Nakagawa, T. Muranaka, Y. Zenitani, and J. Akimitsu, Nature **410**, 63 (2001).

[13] C. Rhodes, J. Stuart, R. Lopez, X. Li, M. Waje, M. Mullings, J. Lau, and S. Licht, J. Power Sources **239**, 244 (2013).

[14] R. B. Kaner, J. J. Gilman, and S. H. Tolbert, Science **308**, 1268 (2005).

[15] H.-Y. Chung, M. B. Weinberger, J. B. Levine, R. W. Cumberland, A. Kavner, J.-M. Yang, S. H. Tolbert, and R. B. Kaner, Science **316**, 436 (2007).

[16] G. Gottstein, *Materialwissenschaft und Werkstofftechnik: Physikalische Grundlagen*, 4th ed. (Springer-Verlag, 2013) pp. 11–114.

[17] K. Momma and F. Izumi, J. Appl. Crystallogr. **44**, 1272 (2011).

[18] "Partial Dislocations and Stacking Faults," `http://dtrinkle.matse.illinois.edu/MatSE584/kap_5/backbone/r5_4_1.html`, accessed: 2021-01-19.

[19] "Partial dislocations in FCC crystals," `http://people.virginia.edu//~lz2n/mse6020/notes/D-partial-fcc.pdf`, accessed: 2021-01-28.

[20] "Deformation Twinning," `https://www.encyclopedia.com/science/dictionaries-thesauruses-pictures-and-press-releases/deformation-twinning`, accessed: 2021-01-20.

[21] "Twinning, Shear Deformation and Martensite Formation," `https://www.tf.uni-kiel.de/matwis/amat/iss/kap_5/illustr/s5_4_3.html`, accessed: 2021-01-28.

[22] V. Läpple, *Wärmebehandlung des Stahls, Grundlagen, Verfahren und Werkstoffe,* (Aufl. Europa Lehrmittel, Haan-Gruiten, 2006).

[23] S. J. La Placa and B. Post, Acta Crystallogr. **15**, 97 (1962).

[24] K. Burke, "The ABC of DFT," `https://dft.uci.edu/doc/g1.pdf`, accessed: 2021-05-23.

[25] J. G. Lee, *Computational Materials Science: An Introduction* (CRC Press, 2011).

[26] G. Kresse, M. Marsman, and J. Furthmüller, "VASP the GUIDE," `https://cms.mpi.univie.ac.at/vasp/vasp.pdf` (), accessed: 2021-05-23.

[27] G. Kresse, M. Marsman, and J. Furthmüller, "History of VASP," `https://cms.mpi.univie.ac.at/vasp/vasp/History_VASP.html` (), accessed: 2021-05-23.

[28] T. Bucko, J. Hafner, and J. G. Angyán, J. Chem. Phys. **122**, 124508 (2005).

[29] A. Togo and I. Tanaka, Scr. Mater. **108**, 1 (2015).